MASTER'S THESIS

Master of Science in Advanced Mathematics and Mathematical Engineering

Title: Communication through coherence in a realistic neuronal model

Author: David Reyner Parra

Advisor: Gemma Huguet Casades

Department: Departament of Mathematics

Academic year: 2019-2020

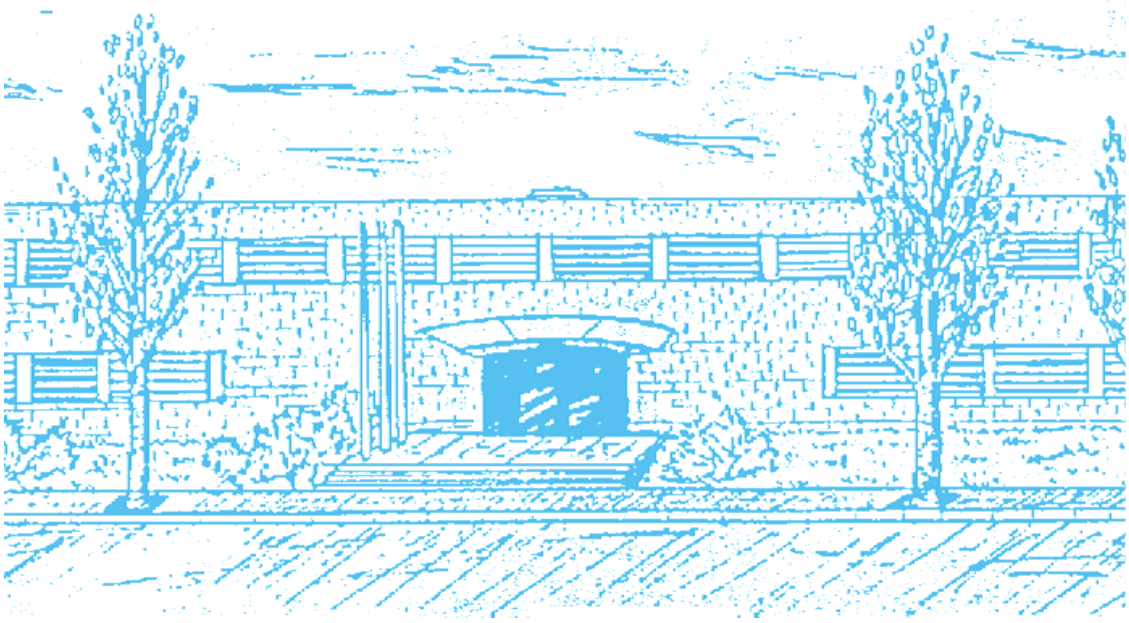

UNIVERSITAT POLITÈCNICA DE CATALUNYA
BARCELONATECH
Facultat de Matemàtiques i Estadística

Universitat Politècnica de Catalunya
Facultat de Matemàtiques i Estadística

Master in Advanced Mathematics and Mathematical Engineering

Master's thesis

Communication through coherence in a realistic neuronal model

David Reyner Parra

Supervised by Gemma Huguet Casades

June, 2020

I would like to give my sincere thanks to my supervisor, Gemma Huguet, for her unconditional devotion to the project, unfailing patience and guidance as well as for finding time during these difficult months. This thesis would not have succeeded in time if it were not for her help.

I would also like to thank her for giving me the opportunity to work as a research support staff, under her own 2019 Leonardo Grant for Researchers and Cultural Creators.

Abstract

Macroscopic oscillations in the brain have been observed to be involved in many brain tasks but their role is not completely understood. The Communication Through Coherence (CTC) theory establishes that neural communication between two neural groups is much effective if the underlying oscillatory activity of both populations is coherent, that is, the input from the emitting population arrives at the peak of excitability of the receiving neural network, promoting an increase in its activity. The oscillators must be therefore phase-locked to accomplish strong communication.

In this project, we study the emerging phase-locking states of a neuronal Excitatory-Inhibitory (E-I) network under external periodic forcing, simulating the input from other neural groups. We use a recent mean-field model, which provides an exact description of the macroscopic activity of a network. The approach that we conduct consists in reducing the dynamics to the phase equation by means of the infinitesimal phase response curve (iPRC), a tool measuring the responses of an oscillator to small perturbations. Then, we locate numerically the phase-locking states, arising from a study of the stroboscopic map associated to the phase equation. Finally, we discuss the implications of the computed phase-locking states on the neuronal communication.

Keywords

Dynamical systems, Computational neuroscience, Phase response curve, Communication through coherence, Phase-locking, Arnold tongues

Contents

1. Introduction

The brain accounts for many vital functions by processing and transmitting electric signals, known as action potentials, from one neuron to another, promoting thus a continuous flux of electrical activity. Interactions between neurons may lead to observable macroscopic oscillatory activity. As an example of this phenomenon, we can take the oscillations in the electrical activity of a neural network due to the action of inhibitory cells (those that prevent the generation of an action potential). The electrical activity of the whole ensemble would then oscillate from a high density of discharged action potentials (inhibitory cells are not active) to a low density (inhibitory cells are active).

Macroscopic neural oscillations were first reported in the late twenties by Hans Berger and further studies have led to a classification concerning frequency bands. The most studied band is known as gamma band, accounting for fast macroscopic oscillations in the brain, ranging from 30 to 100 Hz. It is believed that such gamma oscillations are involved in fundamental cognitive functions such as working memory or perception, yet their role in such processes is still unknown. Some neural disorders, such as epilepsy, have been related to the alteration of gamma rhythms as well.

Neural communication, understood as the capacity of the receiving population (post-synaptic) to respond to the inputs of the emitting population (pre-synaptic), is thought to be affected by such macroscopic oscillations. The Communication Through Coherence (CTC) theory (reviewed in [10]) proposes that communication between two neural groups is more effective when the pre-synaptic input of the sending population reaches the receiving population at its maximum phase of excitability (for instance, when inhibition is not present). That is, the inherent phases to both neural groups must be phase-locked to coherently accomplish communication.

Because of its complexity, the mathematical treatment of a neural network has been addressed from a purely numerical perspective. Starting with the classical *Wilson-Cowan* model (see [16]), the mean-field formulation provides a different approach to modelling, whereby networks are described by the average firing frequency (or *firing rate*). However, these macroscopic descriptions were derived ad-hoc and failed to capture some relevant phenomena, like synchrony. Falling into this category, a novel firing-rate model has been lately derived that gives an exact description of the network dynamics (see ([8]).

In this dissertation we consider a realistic low-dimensional mean-field model (presented in [2]) consisting of a mutually interconnected network of excitatory and inhibitory neurons, accounting for macroscopic gamma oscillations via the classical PING and ING mechanisms. These two mechanisms constitute the models with the minimum requirements to give rise to gamma oscillations: interplay between excitation and inhibition (PING) or only with inhibition (ING). The dynamical study that we aim to conduct is similar in spirit to the work proposed by [11] with a further assumption, which allows great simplifications: the weak coupling hypothesis. We will then explore how the intrinsic phase dynamics of an oscillation, arising either from a PING or a ING mechanism, adapts when it is externally perturbed by a weak periodic stimulus. The goal is to locate the phase-locking states between the neural oscillator and the external periodic input as a function of their coupling strength and period relation.

The present study requires first to examine how a neural oscillator responds to incoming perturbations and the mathematical tool to characterize it is the *phase response curve* (PRC). The weak coupling assumption, which plays a key role throughout this thesis, combined with the PRC tool enables us to reduce the dynamics close to the oscillator to a single equation, known as *phase equation*. Since the perturbation is periodic, we define the so-called *stroboscopic map* for the phase equation, whose fixed

and periodic points correspond to different phase-locking states. For this map we numerically compute the associated rotation number at different amplitudes, giving rise to a very well-known fractal-structured functions called *Devil's staircases*. The location of fixed and periodic points is much clearer from these Devil's staircases. Finally, a bifurcation analysis of the stroboscopic map determines the Arnold tongues, that is, the regions where the different phase-locking states are located in the parameters space of the amplitude strength and frequency of the periodic input.

Our study is organized in the following way. In Section 2 we introduce the network model we will work with. Namely, in Section 2.1 we present the full neuronal network model and the mean-field model, which gives an exact description of the macroscopic dynamics of the network. Section 2.2 gives a brief introduction to the PING and ING mechanisms, supported by some numerical simulations. In Section 2.3 we carry out an analysis of the oscillations that emerge for this reduced model (study based on [15]). Section 3 deals with the mathematical study of the phase-locking states. It is divided in four parts. Section 3.1 presents the usual parametrization of an oscillator by the phase and the reduction to the phase equation for the unperturbed case. Section 3.2 discusses the mathematical (and numerical) treatment of the oscillator's response to weak stimuli. Closely related to the previous one, in Section 3.3 we perturb periodically the oscillator and study the perturbed dynamics through the stroboscopic map and its rotation number. In Section 3.4, we apply a continuation method to locate these phase-locking states and compute the Arnold tongues. In Section 4 we give a brief interpretation of the $1:1$ phase-locking state in the CTC context. Finally, in Section 5 we discuss the results obtained and future work.

2. Neuronal networks and Gamma rhythms

The neurons constitute the basic biological units of the nervous system and are responsible for receiving, processing and transmitting electrical signals. Such electrical signals consist of rapid variations in the membrane potential of the cells and are called action potentials (or *spikes*, because of the shape of such variations over time). Electrical impulses travel from neuron to neuron via synaptic connections. Synapses may be excitatory or inhibitory, depending on whether the emitting neuron (pre-synaptic) leads to an increase or a decrease in the voltage of the receiving neuron (post-synaptic).

Several neuronal models have been developed to mathematically model the evolution of the voltage of a neuron. For a biologically detailed (yet computationally expensive) model we refer to the pioneering Hodgkin-Huxley model (see [5]). A less biologically plausible but more computationally efficient family of neural models is the *Integrate-and-fire* (IF) family (see [6]). Such models consist of a single differential equation describing the membrane potential and a voltage-resetting rule when a preset threshold is surpassed. Because of its simplicity, integrate-and-fire models capture only the fundamental excitability properties of a neuron (e.g. spike timing and response to stimuli) and fail to exhibit many neurocomputational features. The reader is referred to [7] for an interesting comparison between biological plausibility and computational cost of the most widely-known models in neuroscience.

A usual choice, which enables simulations of large-scale neural networks efficiently, is the *quadratic integrate-and-fire* (QIF) model. Its canonical form consists of a single first order quadratic differential equation and a reset rule,

$$\tau \frac{dV}{dt} = V^2 + I\,, \quad \text{if } V \geq V_{\text{th}} \text{ then } V_{\text{reset}} \leftarrow V\,, \tag{1}$$

where V models the membrane potential (voltage) of the neuron and τ is the time constant controlling the rate at which the voltage changes (the larger it is, the slower is the convergence to the asymptotic value). When the voltage reaches the threshold value V_{th}, it is automatically reset to V_{reset}. The resetting rule defines when a neuron has fired a spike. The input current I accounts for external stimuli such us electrical impulses of other neurons to which it is connected via synapses.

When dealing with neural networks of synaptically coupled neurons, the complexity of the network connectivity together with the neuron models make the mathematical analysis more difficult. *Mean-field* models overcome this drawback by describing the macroscopic state of a network in terms of average quantities such as the mean voltage or the mean firing rate of the network (i.e. "spikes per unit of time"). The equations that account for these descriptions are commonly called *firing-rate equations* (FREs). Recently, a set of FRE equations has been derived, reproducing exactly the macroscopic dynamics of a network of all-to-all coupled QIF neurons (see [8] for the derivation). In this project, we consider the low dimensional system studied in [2], that is based on this exact model (we discuss its principal advantages in the following section), which allows for a more treatable description of ensembles of neurons. Next, we present the model, detailing the biological meaning of the macroscopic variables and its parameters.

2.1 The model

We consider a population of N neurons with all-to-all coupling, subdivided into a population of N_e excitatory cells and another one of N_i inhibitory cells, whose individual dynamics are modelled by the following QIF

model

$$\tau \dot{V}_j = V_j^2 + \eta_j + I_j\,, \quad \text{if } V_j \geq V_{\text{th}} \text{ then } V_j = V_{\text{reset}}\,, \quad j = 1, \ldots, N\,, \tag{2}$$

where V_j, as stated before, denotes the voltage of the j-th neuron and I_j is an input current, accounting for external (time-dependent) stimuli and the excitatory/inhibitory synapses of the network. According to the analysis presented in [8], we have to consider $V_{\text{th}} = -V_{\text{reset}} \to \infty$. However, in numerical simulations, we will set them to some (large) fixed value to reproduce the spike timing. The kinetics of equation (2) is governed by the time constant τ, measuring, to a certain extent, how rapid the neural voltage changes (the smaller is the time constant, the faster it changes).

We introduce a certain degree of heterogeneity in the network by considering that each neuron is in a different excitable state. For instance, some neurons may exhibit spiking activity (with higher or lower frequency) and others may remain in a quiescent state (with voltage closer or further from the threshold). Computationally, this is accounted for in the QIF equation (2) by the constant input current η_j. The constant input η_j is chosen from a Lorentzian distribution with half-width Δ and centered at $\bar{\eta}$,

$$L(\eta) = \frac{1}{\pi} \frac{\Delta}{(\eta - \bar{\eta})^2 + \Delta^2}\,. \tag{3}$$

The input current I_j is different depending on which is the receiving population (the excitatory or the inhibitory). It consists of a common external input for all neurons (of that population) and a varying synaptic current. For the excitatory ensemble, the input is expressed as

$$I_e = I_e^{\text{ext}} + \tau_e S_{ee} - \tau_e S_{ei}\,, \tag{4}$$

while for the inhibitory one as

$$I_i = I_i^{\text{ext}} + \tau_i S_{ie} - \tau_i S_{ii}\,. \tag{5}$$

We have omitted the subindex j (labeling a neuron in the population) because all the neurons in the same population receive the same input current. The subscript indicates whether it corresponds to the excitatory (e) or the inhibitory (i) population. The variable S_{ab} models the synaptic connection between the emitting neural ensemble b to the receiving one a, where $a, b \in \{e, i\}$. They can be distinguished between local (from a population to itself) and non-local (with different emitting and receiving populations). The synapses, independently whether they are excitatory or inhibitory, are modelled by a linear differential equation with exponential decay

$$\tau_s \dot{S}_{ab} = -S_{ab} + J_{ab} r_b\,, \tag{6}$$

where $a, b \in \{e, i\}$. The time constant τ_s controls the velocity at which the variable S_{ab} approaches its asymptotic state. The quantity r_b is a theoretical measure that counts the number of spikes of a neural ensemble at a given time. The parameter J_{ab} measures how strong is the connection from population b to population a (the stronger, the more sensitive is population a to the activity of population b).

Thus far we have described with some detail the microscopic dynamics of the network, resulting in a high-dimensional model whenever N is sufficiently large. We now describe the network through the aforementioned exact firing-rate description (see [8]), that is, in terms of macroscopic relevant quantities such as the firing rate - a measure of the electrical activity of a neural ensemble characterized by the number of spikes per unit of time - and the mean membrane potential. As it has been suggested before, the advantages of such a description are twofold: it reduces the high dimensionality of the miscroscopic approach of the network and it provides an exact description of the macroscopic dynamics of the network of

QIF neurons. The model has been derived in the thermodynamic limit, that is, assuming that the number of neurons N tends to infinity.

The dynamics of the macroscopic firing-rate r and mean voltage V variables are described by a set of two differential equations

$$\begin{aligned} \tau \dot{r} &= \frac{\Delta}{\pi\tau} + 2rV \,, \\ \tau \dot{V} &= V^2 + \bar{\eta} + I(t) - (\tau\pi r)^2 \,. \end{aligned} \tag{7}$$

There are three parameters: the half-width Δ and the center $\bar{\eta}$ coming from the distribution (3) and the time constant τ, controlling the speed dynamics to the steady state. Including equations (6) for the synapses, the low-dimensional mean-field model consists then of a set of four differential equations for the excitatory population,

$$\begin{cases} \tau_e \dot{r}_e = \dfrac{\Delta_e}{\pi\tau_e} + 2r_e V_e \,, \\ \tau_e \dot{V}_e = V_e^2 + \bar{\eta}_e + I_e - (\tau_e \pi r_e)^2 \,, \\ \tau_{s_e} \dot{S}_{ee} = -S_{ee} + J_{ee} r_e \,, \\ \tau_{s_e} \dot{S}_{ei} = -S_{ei} + J_{ei} r_i \,, \end{cases} \tag{8}$$

and another identical set for the inhibitory one,

$$\begin{cases} \tau_i \dot{r}_i = \dfrac{\Delta_i}{\pi\tau_i} + 2r_i V_i \,, \\ \tau_i \dot{V}_i = V_i^2 + \bar{\eta}_i + I_i - (\tau_i \pi r_i)^2 \,, \\ \tau_{s_i} \dot{S}_{ie} = -S_{ie} + J_{ie} r_e \,, \\ \tau_{s_i} \dot{S}_{ii} = -S_{ii} + J_{ii} r_i \,, \end{cases} \tag{9}$$

The variables r_a and V_a, with $a \in \{e, i\}$, denote the firing rate activity and the mean membrane potential of the population a, respectively. Notice that these two neural populations are coupled via the non-local synapses. Depending on which population activates, this can have different effects onto the receiving population: an excitatory population increases the mean membrane potential of the neural populations to which it is connected (and, in consequence, its firing rate) whereas an inhibitory population decreases their mean membrane potentials (and therefore also their firing activity). In system (8) - (9), as for the microscopic approach, the input from the population itself and other neural groups is described by the terms I_e and I_i in the equations for the variables V_e and V_i, respectively. The total input current for the excitatory population is given by

$$I_e = I_e^{\text{ext}} + \tau_e S_{ee} - \tau_e S_{ei} \,, \tag{10}$$

and for the inhibitory one, by

$$I_i = I_i^{\text{ext}} + \tau_i S_{ie} - \tau_i S_{ii} \,. \tag{11}$$

We have considered two different Lorentzian distributions: one for the excitatory population (with half-width Δ_e and center $\bar{\eta}_e$) and the other for the inhibitory one (with parameters Δ_i and $\bar{\eta}_i$). In practice,

we assume that the intrinsic potential of both excitatory and inhibitory neurons is distributed following the same Lorentzian function and thus, $\Delta_e = \Delta_i$ and $\bar{\eta}_e = \bar{\eta}_i$.

In Figure 1 we present a representation of the excitatory-inhibitory neural network described by system (8) - (9) and their excitatory and inhibitory synaptic connections.

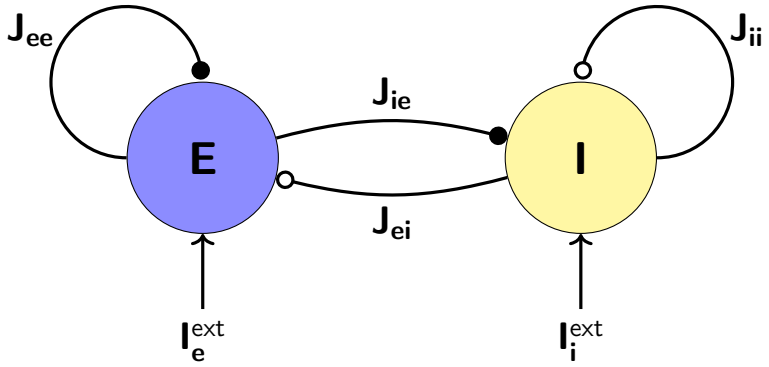

Figure 1: Scheme of a neural network coupled via excitatory and inhibitory synapses (E-I network). Excitatory synapses are depicted by curved lines with a black-filled circle pointing at the receiving population. For the inhibitory ones, these are represented by curved lines with empty circles.

2.2 Emerging rhythms: PING and ING interactions

Macroscopic oscillations of neural activity are widely-known to emerge in different brain regions. Such oscillations have been classified in distinct bands according to their frequencies. Of this frequency division, the most studied rhythmic band is known as gamma band and covers those fast macroscopic brain oscillations with frequencies ranging, approximately, from 30 to 100 Hz. Such fast rhythmic patterns have been observed in several cognitive brain functions, yet little is known about their underlying mechanisms and their exact role in the brain tasks. Several studies on gamma-frequency oscillations have provided the fundamental neurological requirements to generate them: either from an interplay of an excitatory (E) and inhibitory (I) populations or from a single inhibitory population with self-feedback. These two processes are referred to as PING and ING mechanisms, respectively, and represent the classical underlying models to generate and explain such gamma oscillations. There are other mechanisms that could induce gamma rhythms as well but they are beyond of the scope of this project. Next, we describe the main features of these two processes to generate gamma-oscillations in a very succinct manner. We refer to [1] for a further discussion and a detailed biological interpretation supporting gamma oscillations.

The PING (Pyramidal Interneuron Network Gamma) mechanism consists of two ensembles of neurons, one of excitatory (pyramidal) cells and the other one of inhibitory (interneuron) cells, interconnected synaptically. With sufficiently strong and persistent external excitatory drive (i.e. I_e^{ext}), the pyramidal neurons become more excitable, increasing the average voltage of the population and thus discharging spikes at a much higher rate. This rise in voltage promotes a positive input onto the inhibitory population which, in turn, triggers a reciprocal inhibiting feedback onto the excitatory cells. Such inhibition makes the E-population less receptive to the external drive until its effect decays, starting again the excitation-inhibition loop. This generates a self-sustained macroscopic oscillatory activity.

Figure 2 serves first to compare both reduced and full neural models and second, to give an example of gamma oscillations generated by a PING interaction. Red and blue lines denote the oscillatory time evolution of the excitatory and inhibitory firing rate variables r_e and r_i, respectively. The firing activity of a large-scale simulation of a network of 10.000 QIF neurons (5000 pyramidal neurons and 5000 inhibitory neurons) has been also rendered (in black); it has been computed by averaging the number of spikes in a preceding time window of size $\delta t = 8 \cdot 10^{-2}$. One may observe that the periodic behaviour in the large-scale simulation agrees almost perfectly with the one predicted by the reduced mean-field system (8) - (9). We attribute this small difference in the firing rate variables to either a small/large time-preceding window when counting spikes or to the number of neurons N that has not been chosen large enough (recall that the model presented in [8] is exact in the thermodynamic limit, i.e. $N \to \infty$).

The excitatory external drive I_e^{ext} applied to both the reduced and the full models has been illustrated in the bottom panel. The set of parameters for such a simulation has been taken from [2] and, unless otherwise stated, will be considered hereafter for the analysis of the PING case

$$\textbf{PING} \quad \begin{cases} \textbf{Time Constants:}\ \tau_e = 10\,,\ \tau_i = 10\,,\ \tau_{s_e} = 1\,,\ \tau_{s_i} = 1 \\ \textbf{Half-Width:}\ \eta_e = -5\,,\ \eta_i = -5 \\ \textbf{Synaptic Strength:}\ J_{ee} = 0\,,\ J_{ei} = 15\,,\ J_{ie} = 15\,,\ J_{ii} = 0 \\ \textbf{External Input:}\ I_e^{\text{ext}} = 10\,,\ I_i^{\text{ext}} = 0 \end{cases} \tag{12}$$

The ING (Interneuron Network Gamma) rhythm consists of a single population of inhibitory (interneuron) cells with self-inhibiting feedback. When the external current I_i^{ext} applied on the inhibitory population is relatively strong, the interneuron cells fire actively and the resulting postsynaptic current, after a time proportional to τ_{si} (time constant governing the kinetics of the S_{ii} synapses), inhibits the population itself for a while. The inhibition diminishes the activity of the population by making cells less excitable (average voltage decreases). After the inhibition dies out, the external drive kicks again and the cycle repeats. The time constant is key to have ING oscillations, otherwise inhibition would act immediately, causing cells not reaching the threshold to fire and thus bringing the activity to some steady state (no periodic behaviour).

A similar set of parameters as in Figure 2 leads to ING high-frequency oscillations, captured also by the reduced model. Figure 3 supports again that the mean-field approach given by system (8) - (9) captures quantitatively the essential dynamical states of the full network of QIF neurons. Indeed, the firing rate variables (red and blue lines) agree perfectly with the average firing activity of the whole network. The external drive (now applied to the inhibitory cells) has a similar form as in Figure 2 but with a higher-frequency sinusoidal function $s(t)$. This is so because the gamma rhythm for the ING case oscillates at a much higher frequency ($T^* \approx 8.522$ ms with frequency 117 Hz) than for the PING case ($T^* \approx 20.811$ ms). In fact, this frequency difference holds in general: PING and ING mechanisms give rise to slow and fast gamma oscillations, respectively. As for the PING process, the set of parameters showing ING oscillations has been taken from [2] and will be used throughout the following sections when dealing with this process

$$\textbf{ING} \quad \begin{cases} \textbf{Time Constants:}\ \tau_e = 10\,,\ \tau_i = 10\,,\ \tau_{s_e} = 1\,,\ \tau_{s_i} = 1 \\ \textbf{Half-Width:}\ \eta_e = -5\,,\ \eta_i = -5 \\ \textbf{Synaptic Strength:}\ J_{ee} = 0\,,\ J_{ei} = 0\,,\ J_{ie} = 0\,,\ J_{ii} = 15 \\ \textbf{External Input:}\ I_e^{\text{ext}} = 25\,,\ I_i^{\text{ext}} = 25 \end{cases} \tag{13}$$

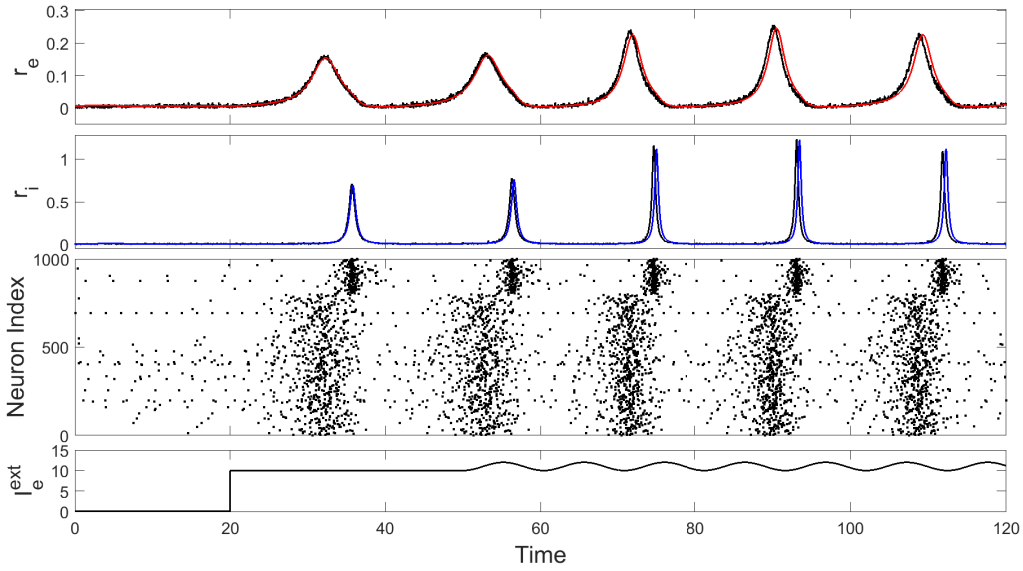

Figure 2: Comparison between the low-dimensional mean-field system (8) - (9) and a large-scale numerical simulation of the whole network for the PING interplay. First two top panels compare the firing rate of the excitatory (red) and the inhibitory (blue) populations, described by the mean-field model, with the collective firing activity of the simulated dynamics of a network of QIF neurons (black). Third panel shows a raster plot of 1000 randomly selected neurons: the first 800 are excitatory and the last 200 inhibitory. In the last panel we draw the external current applied on the excitatory neurons, I_e^{ext}: a step function up to $t = 50$ smoothly joined with a positive sinusoidal function $s(t) = 1 + \cos\left(\frac{2\pi(t-50)}{T} + \pi\right)$, where $T = 0.5\,T^*$ and $T^* \approx 20.811$ ms (≈ 48 Hz) is the period of the PING oscillations at time interval $[20, 50]$. Parameters: $N_e = 5000$, $N_i = 5000$, $\tau_e = \tau_i = 10$, $\Delta_e = \Delta_i = 1$, $\eta_e = \eta_i = -5$, $\tau_{se} = \tau_{si} = 1$, $J_{ee} = J_{ii} = 0$, $J_{ei} = J_{ie} = 15$, $I_i^{\text{ext}}(t) = 0$ for all time and $I_e^{\text{ext}}(t) = 10$ for $20 \leq t \leq 50$, afterwards we add the function $s(t)$.

Notice that the activity of the excitatory population decays since it has been isolated from any synaptic current (that is, $J_{ei} = J_{ie} = 0$). So, this choice of parameters defines indeed an ING interaction.

2.3 Characterization of gamma oscillations

In this section we proceed to characterize the oscillations for PING as a function of the constant external current in terms of the relative phase between the firing rate of the excitatory and inhibitory populations. Here, by relative phase we mean the time difference between the maximum of inhibition and the maximum of excitation. The study that we carry out along this section is based on [15], though we apply it to the reduced model instead of the full microscopic one.

We first need to determine for which values of $(I_e^{\text{ext}}, I_i^{\text{ext}})$ the model (8) - (9) shows an oscillatory behaviour. As observed in Figures 2 and 3, with a strong enough constant drive the system (8) - (9) transitions from resting state to an oscillatory regime. From the viewpoint of dynamical systems we say that the system has undergone a bifurcation - a qualitative change in the underlying dynamics when a parameter is varied (in our case when I_e^{ext} or I_i^{ext} are varied). There are several types of bifurcations giving

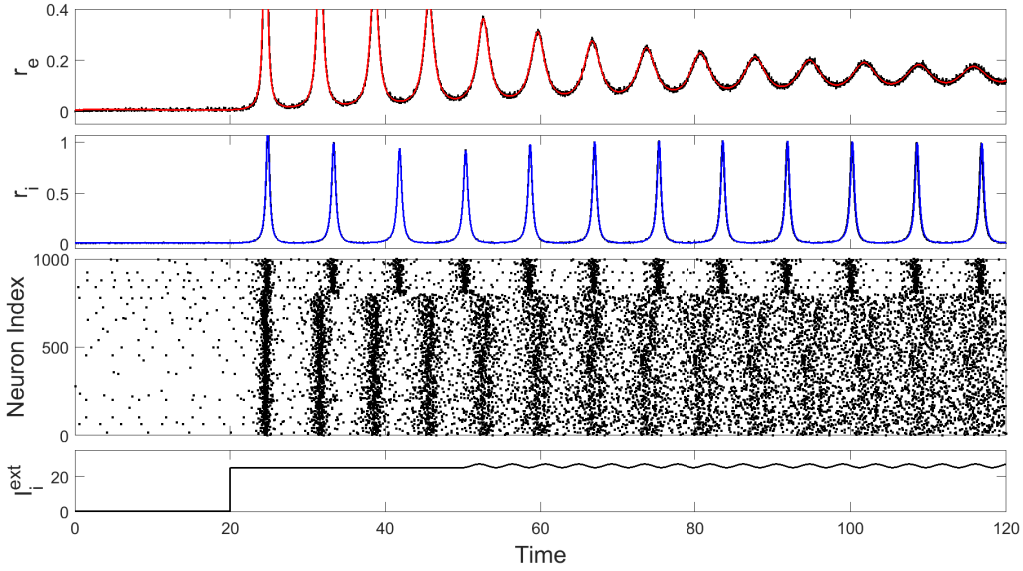

Figure 3: Comparison between the low-dimensional mean-field system (8) - (9) and a large-scale numerical simulation of the whole network for the ING interplay. First two top panels compare the firing rate of the excitatory (red) and the inhibitory (blue) populations, described by the mean-field model, with the collective firing activity of the simulated dynamics of a network of QIF neurons (black). Third panel shows a raster plot of 1000 randomly selected neurons: the first 800 are excitatory and the last 200 inhibitory. In the last panel we draw the external current applied on the inhibitory neurons, I_i^{ext}: a step function up to $t = 50$ smoothly joined with a positive sinusoidal function $s(t) = 1 + \cos\left(\frac{2\pi(t-50)}{T} + \pi\right)$, where $T = 0.5\,T^*$ and $T^* \approx 8.522$ ms (≈ 117 Hz) is the period of the ING oscillations at time interval $[20, 50]$. Parameters: $N_e = 5000$, $N_i = 5000$, $\tau_e = \tau_i = 10$, $\Delta_e = \Delta_i = 1$, $\eta_e = \eta_i = -5$, $\tau_{se} = \tau_{si} = 1$, $J_{ee} = J_{ei} = J_{ie} = 0$, $J_{ii} = 15$, $I_e^{\text{ext}}(t) = 25$ for $t \geq 20$ and $I_i^{\text{ext}}(t) = 25$ for $20 \leq t \leq 50$, afterwards we add the function $s(t)$.

rise to oscillations but the most common ones are the Hopf bifurcation and the Saddle-Node on Invariant Cycle (SNIC) bifurcation. Without entering into further details, the main difference of such bifurcations is that oscillations rising from a Hopf are born with frequency bounded away from zero (finite period), whereas the frequency of those emerging from a SNIC approaches to zero as we move closer to the bifurcation point (i.e. are born with infinite period). We refer to [3] for a bifurcation analysis of the classical Morris-Lecar model where these two types of bifurcations are well-explained.

The transition resting-to-oscillation has been shown to occur via a Hopf bifurcation in both gamma-generating mechanisms, by varying either the current I_e^{ext} (resp. I_i^{ext}) or the heterogeneity Δ_e (resp. Δ_i) for the PING (resp. ING) case (see [2]). On this basis, we have conducted for the PING interplay a two-parameter bifurcation diagram by varying both currents I_e^{ext} and I_i^{ext}. To do so we have made use of the numerical bifurcation analysis toolbox MatCont (a Matlab continuation package). We first have determined a Hopf bifurcation point (starting from the work [2]) and after that we have continued the bifurcation either forward and backward. The resulting bifurcation diagram is plotted in Figure 4. The Hopf bifurcation curve (dark blue line) separates the (I_e^{ext}, I_i^{ext})-plane between a gamma-oscillation region (blue) and a resting region. Along this curve, Generalized Hopf bifurcations (or Bautin bifurcations) have been found (red circles). Briefly a Generalized Hopf is a bifurcation where the Hopf bifurcation changes from

being supercritical to subcritical (or vice versa), that is, the emerging limit cycle is no longer stable (resp. unstable) and becomes unstable (resp. stable). For further information on Generalized Hopf bifurcations we refer the reader to [4].

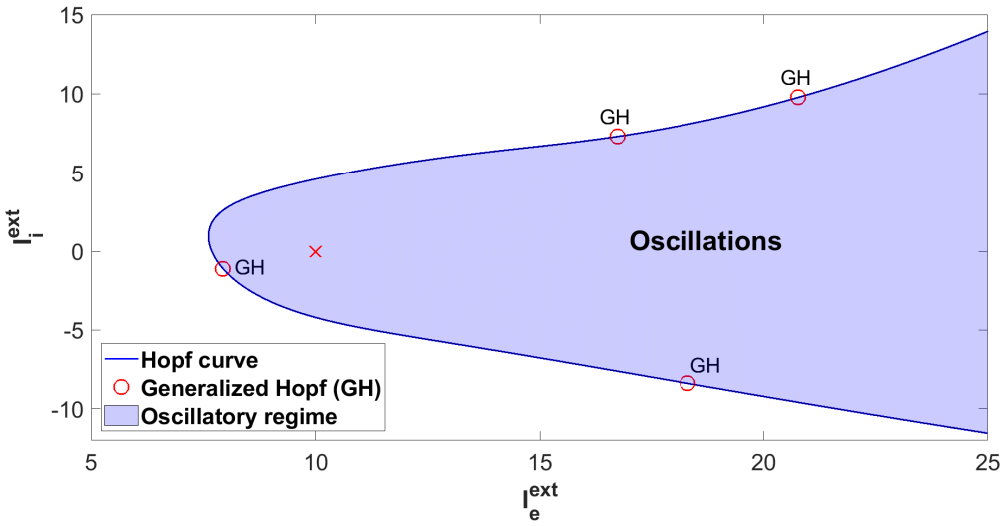

Figure 4: Two-parameter bifurcation diagram with excitatory current I_e^{ext} in the x-axis and inhibitory current I_i^{ext} in the y-axis. Dark blue line is the Hopf bifurcation curve and delimits the region where one finds macroscopic oscillations. Red circles denote the (codimension 2) Generalized Hopf bifurcations (i.e. the periodic orbit born in the Hopf curve changes its stability at this bifurcation point). Red x-mark indicates the point $(I_e^{\text{ext}}, I_i^{\text{ext}})$ corresponding to the PING set (12).

To study the relative phase between the inhibition and the excitation we consider a fixed value of the external inhibitory current I_i^{ext}, $I_i^{\text{ext}} = 0$, and we increase the excitatory one I_e^{ext} from 0 to 15. This interval, according to Figure 4, covers the progression towards the oscillatory region. By forward integration for sufficiently large time we will converge to a stable periodic orbit, whenever it exists. Once the orbit has been located, its period will vary as the excitatory current I_e^{ext} is gradually modulated. In Figure 5A we plot the frequency of the emerging limit cycle as a function of the current injected onto the E cells (green curve). There are two aspects related to that frequency that should be emphasized: first, the frequency is bounded away from zero (characteristic of a Hopf bifurcation) and second, the frequency ranges from $30 \sim 70$ Hz, indicating gamma-type oscillations.

We have also computed the integral mean values of the firing rate of both populations, that is,

$$R_e := \frac{1}{T^*}\int_0^{T^*} r_e(s)\,ds\,, \qquad R_i := \frac{1}{T^*}\int_0^{T^*} r_i(s)\,ds\,, \tag{14}$$

where T^* is the oscillation period, as we gradually increase the parameter I_e^{ext}. Equations (14) give an estimate, in average, of the frequency at which the ensemble of neurons triggers a spike. Figure 5A shows these two average quantities as a function of the input (red-dashed line for the excitatory cells and the blue-dashed line for the inhibitory ones). Both functions approach to the frequency oscillation curve as the injected stimulus I_e^{ext} increases. In Figure 5B we plot the time difference (blue curve) and the relative phase (orange curve) between the inhibition and the excitation in one cycle $[0, T^*]$. By relative phase we

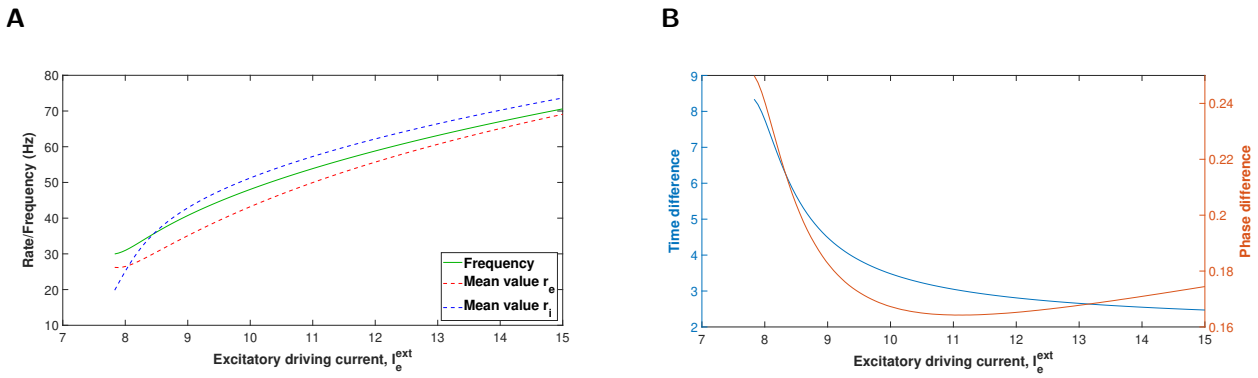

Figure 5: Increasing the external excitatory stimulus I_e^{ext} leads to higher-frequency oscillation and a decrease in the relative phase between inhibition and excitation. (**A**) Frequency oscillation (green) and integral mean values of the firing rate r_e (dashed-red line) and r_i (dashed-blue line). Note that the frequency ranges around $30 \sim 70$ Hz. (**B**) The time difference (blue line) and relative phase (orange line) between inhibition and excitation. The difference is taken at the peaks of r_e and r_i in one cycle. Other parameters are as in (12).

mean the time difference normalized by the period. Increasing the external input onto the E cells causes a reduction on the relative phase and thus a shortening of the latency period of inhibition over excitation.

Similar results are obtained when we vary the constant external drive onto the inhibitory cells, I_i^{ext}. For this study we set the excitatory input I_e^{ext} to 15 and we decrease the inhibitory one from 10 to -5 (see Figure 4). Note that we are initially in the non-oscillatory region and as we decrease the input we go further into the oscillatory regime. As before, the integral mean firing rates R_e and R_i (dashed lines in Figure 6A) oscillate with a frequency approaching to that of the macroscopic oscillations (green line in Figure 6A). Decreasing I_i^{ext} does not have much effect on the oscillation frequency as happened with the previous case (the frequency does not vary so much). By contrast, varying I_i^{ext} implies an increase in the relative phase, widening the inhibition-to-excitation latency (i.e. the inactive period after inhibition acts on excitation is increasingly longer).

Thus far we have presented the model we will work with and the PING/ING oscillations emerging from it for certain sets of parameters. We have shown that the macroscopic model, as proved originally in [8], reproduces exactly the macroscopic dynamical behaviours of large neuronal ensembles (see Figures 2 and 3). We have also analysed for which external inputs I_e^{ext} and I_i^{ext} gamma oscillations arise and how the relative phase between inhibition and excitation varies as a function of such inputs. Now, we aim to study the different phase-locking patterns that these oscillatory neural populations may exhibit when are externally perturbed by a weak periodic stimulus. Such patterns are actually mathematical relations between the frequency of the oscillator and that of the external stimulus. As an example, synchronization between oscillator and stimulus would be a particular phase-locked state. In the next sections we explore the emergence of such relations for both PING and ING mechanisms.

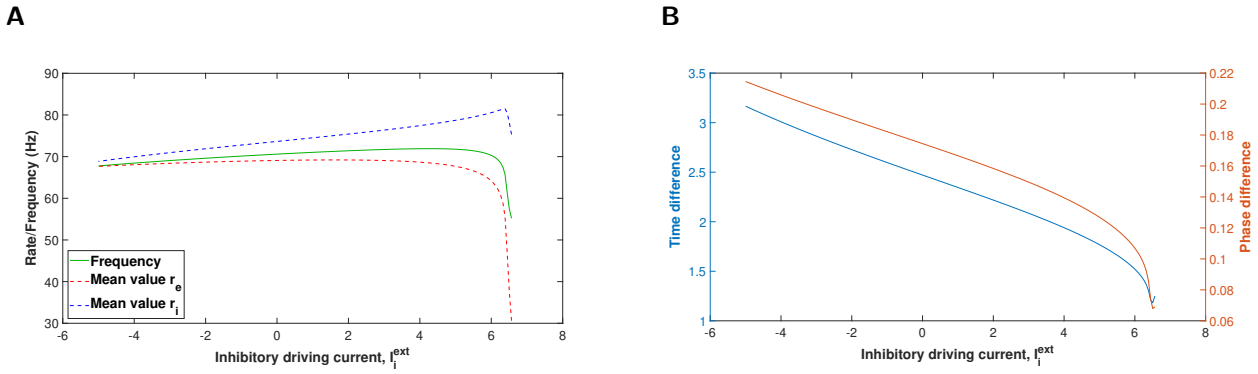

Figure 6: Decreasing the external inhibitory stimulus I_i^{ext} (from right to left) leads to oscillation frequency a little bit higher and an increase in the relative phase between inhibition and excitation. (**A**) Frequency oscillation (green) and integral mean values of the firing rate r_e (dashed-red line) and r_i (dashed-blue line). The frequency ranges around $50 \sim 70$ Hz. (**B**) The time difference (blue line) and relative phase (orange line) between inhibition and excitation. The difference is taken at the peaks of r_e and r_i in one cycle. Other parameters are as in (12).

3. Mathematical analysis of Phase dynamics

In this section we study the response of the oscillator described by the low dimensional firing-rate model (8) - (9) under weak periodic stimulus. The study that we carry out in this section is valid for any n-dimensional oscillator so, we present it in the more general framework. In particular, this study will allow us to explore the possible phase relations between the neural oscillator and an external periodic stimulus.

3.1 Phases of an oscillator and reduction to phase equation

Either in the PING or in the ING mechanism, for an adequate set of parameters, the system of differential equations (8) - (9) has a hyperbolic asymptotically stable limit cycle Γ, of period T^*, that can be parametrized by the function $\gamma : \mathbb{R} \to \mathbb{R}^n$, i.e. a solution of the system such that $\gamma(t + T^*) = \gamma(t)$, for any $t \in \mathbb{R}$ and positive constant T^*, attracting all nearby orbits. Typically, this stable limit cycle is referred to as an oscillator.

Any oscillator can be parametrized by a single phase variable θ measuring the integration time elapsed (modulo T^*) when starting from a reference point on the periodic orbit, pinpointed by a reference phase zero $\theta_0 = 0$ (i.e. $\theta(t) = t + \theta_0 \mod T^*$). Of course, the phase variation over time is expressed by a very simple ordinary differential equation

$$\frac{d\theta}{dt} = 1\,. \tag{15}$$

In single neuron models, the zero phase is established at the moment of the spike, that is, when the neuron's voltage is at its highest value. In population models, we decide to locate the zero phase at the peak of the neuron's voltage counterpart, the average variable describing the mean membrane potential, V_e for PING and V_i for ING.

The phase variable θ describes uniquely a point on the oscillator via the periodic solution, i.e. $\gamma(\theta(t)) = \gamma(t) = x$, $x \in \mathbb{R}^n$. In Figure 7 we illustrate how the phases on the circle $[0, T^*]/0 \sim T^*$ (left panel) are mapped onto a set of points on the limit cycle for the PING case (right panel) by $\gamma(\theta(t))$. If, for instance, we want to determine the point with phase $T^*/4$, we integrate the whole system (8) - (9) starting from the point with phase zero (that has been previously set to the peak of the excitatory mean membrane potential V_e for the PING case) for a time $T^*/4$. The final integration point is marked with "$\times$" as well as the phase. For the inverse, we introduce the phase function $\Theta(x) : \mathbb{R}^n \to \mathbb{R}$, that maps each point on the oscillator to its corresponding phase.

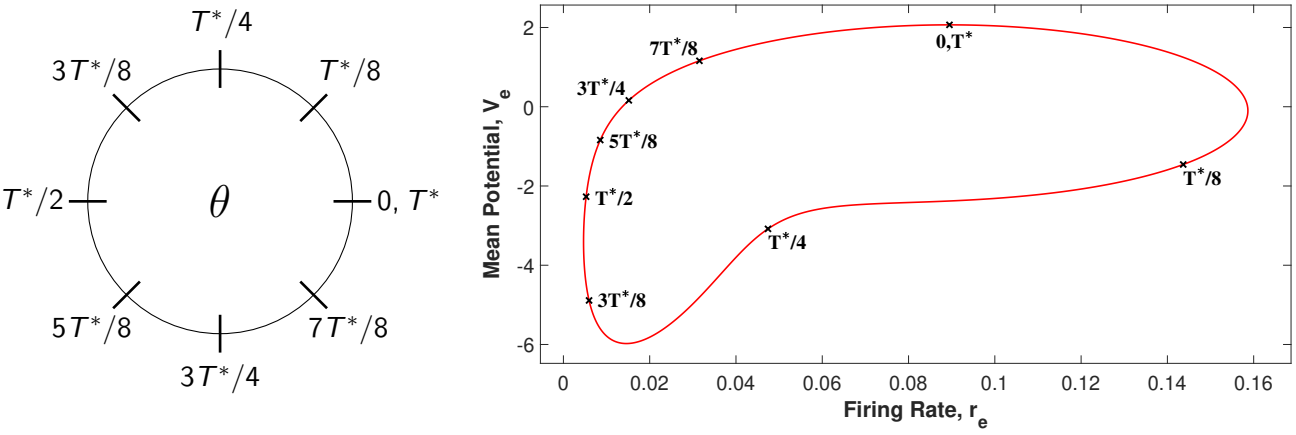

Figure 7: Illustration of how phases of the circle determine uniquely the points on the limit cycle for the PING model. (Left panel) Plot of equidistributed phases on the circle $[0, T^*)$. (Right panel) Projection of the periodic orbit onto the (r_e, V_e)-plane with the points on the limit cycle corresponding to such phases.

If the limit cycle Γ is asymptotically stable (i.e. solutions with initial conditions near the limit cycle converge to $\gamma(t)$), the phase function can be defined not only for those points lying on the limit cycle but also for those that belong to its basin of attraction (i.e. the set of initial points whose orbits eventually approach to $\gamma(t)$). Let x_0 be a point on the limit cycle and y_0 a point on its basin of attraction. Let $x(t)$ and $y(t)$ be two solutions of system (8) - (9) starting at x_0 and y_0, respectively. If $\|x(t) - y(t)\| \overset{t\to\infty}{\longrightarrow} 0$, then we say that the asymptotic phase of y_0 is the same as that of x_0, i.e. $\Theta(y_0) = \Theta(x_0)$. The set of points with the same asymptotic phase is called *isochron*. Actually, the isochrons of an oscillator are, by definition of asymptotic phase, the level curves of the phase function $\Theta(x)$, i.e. $\Theta(x) = k$, for k constant.

Thus far, we have an equivalence between points on an oscillator and phases. Even more, we know that the phase dynamics is very simple (equation (15)). This motivates the study of the oscillator by means of reducing the dynamics to a one-dimensional differential equation (instead of an n-dimensional set of ODEs), called *phase equation*. Such a reduction will be essential in Section 3.3 for studying perturbations of an oscillator and phase-locking.

3.2 Infinitesimal PRC and the Adjoint method

In this section we explain how the periodic orbit is affected when a perturbation is applied and how the response is quantified. As we shall see in Section 3.3, the strength of such perturbation is crucial for the study that follows.

Suppose we have an autonomous system of differential equations $\dot{x} = F(x)$, where $F : \mathbb{R}^n \to \mathbb{R}^n$ is the associated vector field, and that it has a T^*-periodic orbit denoted by Γ and parametrized by γ. Now, take a point x on the periodic orbit with corresponding phase $\Theta(x) = \theta$. Let us assume that a brief input (not necessarily weak) kicks the oscillator at the point x. The trajectory is displaced out of the limit cycle and eventually will be attracted again, approaching a point with a different phase. The new phase may be advanced or delayed with respect to the original one for the unperturbed system (i.e. the phase is reset).

To get a better grasp of what advancing and delaying phases of an oscillator really means, Figure 8 illustrates the main ideas of phase resetting. In Figure 8 we consider a trajectory along the limit cycle of the unperturbed system (8) - (9) with parameters in (12) (solid red line in the upper panel and blue in the middle one) and we perturb it with an external brief square current pulse of amplitude $A = 1.2$ (bottom panel) applied to the macroscopic variables V_e (upper panel) and V_i (middle panel) in two different trials. The dashed red (blue) line, representing the perturbed solution, initially coincides with the unperturbed one until the brief stimulus kicks it, making the oscillator to advance (delay) the phase (compare the peak timing of both solutions in Figure 8 for either the advanced and/or the delayed case).

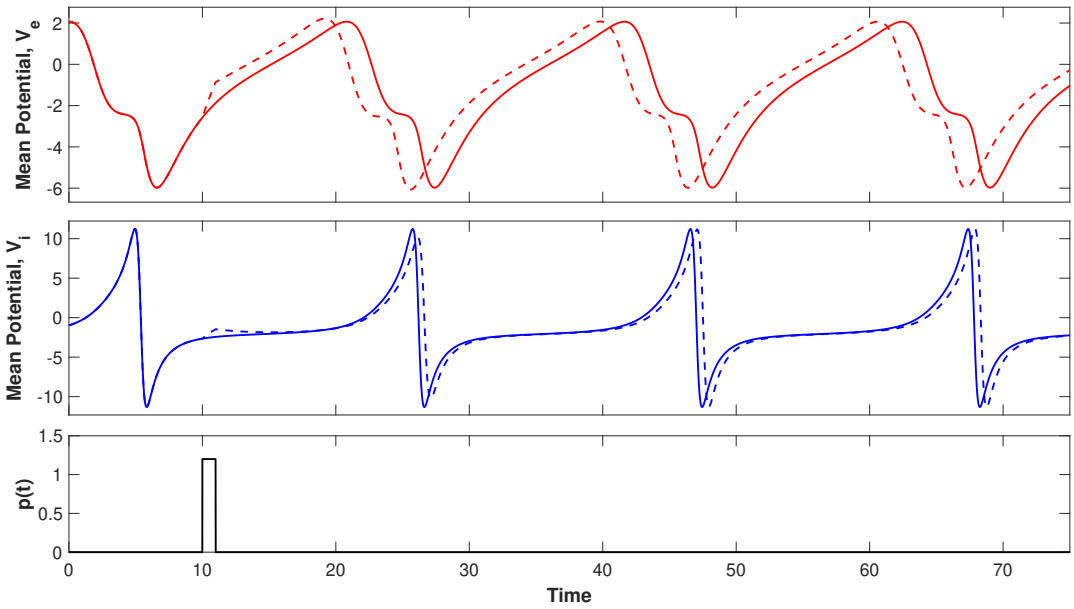

Figure 8: Example of a (Upper panel) phase advance and (Middle panel) phase delay after a brief stimulus. In upper and middle panels, solid lines correspond to the excitatory mean voltage V_e (red line) and inhibitory mean voltage V_i (blue line) of the periodic solution. Dashed lines correspond to time series of V_e (red) and V_i (blue) of the perturbed solution. (Bottom panel) An external square current pulse of length 1 ms with amplitude $A = 1.2$ starting at $t = 10$ ms is applied to the macroscopic variables V_e and V_i in two different trials.

Remark: The perturbed system consists in the same set of equations (8) - (9), adding the term $\tau_e Ap(t)$ (resp. $\tau_i Ap(t)$) to the total excitatory input current (10) (resp. to the total inhibitory input current (11)), where $Ap(t)$ is the external perturbation and A is the strength/amplitude of such perturbation.

We remark that the phase-resetting depends on the point (or phase) of the oscillator that receives the external kick; an equal applied perturbation does not prompt the same phase shift on the oscillator. Then, in order to quantify how a perturbation shifts the phase of an oscillator as a function of the phase at which it is received, we introduce the *phase response curve* (PRC). The PRC is a mathematical tool that measures the difference between the new phase after the stimulus and the old one, that is,

$$PRC(\theta) = \theta_{\text{new}} - \theta\,, \quad \forall\, \theta \in [0, T^*)\,. \tag{16}$$

When the PRC is positive (negative) the phase is advanced (delayed). The impact of the perturbation on the phase is measured by the magnitude of the PRC. Thus, the larger it is (in absolute value) the greater is the impact on the oscillator.

The phase response curve can be computed experimentally (or numerically) by injecting external input and controlling the timing of the next peak and compare it with the unperturbed one. If it occurs earlier then the phase is advanced, otherwise it is delayed.

There are some particular cases where we can obtain a semi-analytical expression of the PRC up to first order. This is the case when the perturbation is infinitesimally small (a pulse). Let us consider $x_0 \in \mathbb{R}^n$ a point on the limit cycle Γ such that $\Theta(x_0) = \theta$. Take now $\varepsilon > 0$ and consider a pulse of strength ε that displaces the trajectory from the point x_0 to a point $x_0 + \Delta x$, where $\Delta x << 1$. The new phase is then $\Theta\big(x_0 + \Delta x\big) = \theta_{\text{new}}$. If we now conduct a Taylor expansion around x_0 we have

$$\theta_{\text{new}} = \Theta\big(x_0 + \Delta x\big) = \Theta(x_0) + \nabla\Theta(x_0)\cdot \Delta x + \mathcal{O}\Big(\big(\Delta x\big)^2\Big)\,. \tag{17}$$

Here we are assuming that the phase function $\Theta(x)$ is regular enough. For small perturbations $\varepsilon << 1$ we have $\Delta x << 1$ and the PRC is approximated to first order by the gradient of the phase function

$$PRC(\theta) = \theta_{\text{new}} - \theta \approx \nabla\Theta(x_0)\cdot \Delta x\,. \tag{18}$$

The function $Z(\theta) := \nabla\Theta(\gamma(\theta))$, with $\theta \in [0, T^*)$, is called the infinitesimal PRC (iPRC). Notice that, the i-th component of the vector $Z(\theta)$ provides the phase shift due to a perturbation acting in the direction of the i-th variable (i.e. $\Delta x = \vec{e}_i$, where $\vec{e}_i$ is the i-th element of the canonical basis in $\mathbb{R}^n$).

Therefore, if we manage to compute the gradient of the phase function then we would be able to know how our oscillator responds to weak pulsatile perturbations. In general, this is a difficult task since we do not know, a priori, the phase function $\Theta(x)$. That said, for small perturbations there is indeed a way to compute $\nabla\Theta(x)$ for $x \in \Gamma$: the Adjoint method. We present it below.

Adjoint Method: Let us assume that F and γ are as described at the beginning of Section 3.2. The iPRC, $Z(t) \in \mathbb{R}^n$, is a periodic solution of the following linear system of differential equations with periodic coefficients

$$\frac{dZ}{dt} = -DF^T\big(\gamma(t)\big)\, Z\,, \tag{19}$$

where $DF\big(\gamma(t)\big)$ is the linearization of the system around the limit cycle Γ. The adjoint equation (19) is subject to the normalization condition

$$Z(t)\cdot F(\gamma(t)) = 1\,. \tag{20}$$

The proof of this result is given in the Appendix A.

In Appendix A we present a method to solve the Adjoint equations efficiently that we have applied to our setting in order to obtain the iPRC vector $\nabla\Theta(\gamma(\theta))$. Figure 9 shows the infinitesimal phase response curves for the firing rate variables (panel **A**), the mean membrane potential ones (panel **B**) and for both excitatory and inhibitory synapses (panels **C** and **D**, respectively) for the PING setting. With red lines we illustrate variables in the excitatory population while with blue the ones in the inhibitory population.

Remark: When we refer to the infinitesimal phase response curve of a certain variable, we mean that the perturbation acts in the direction of that variable. For instance, the iPRC for the excitatory firing rate variable r_e means that $\Delta x = \vec{e}_1$. Similar for the remaining 7 variables. For the sake of clarity we write $iPRC_X$, with $X \in \{r_e, V_e, S_{ee}, S_{ei}, r_i, V_i, S_{ie}, S_{ii}\}$, to refer to the infinitesimal PRC in the direction of the corresponding variable X.

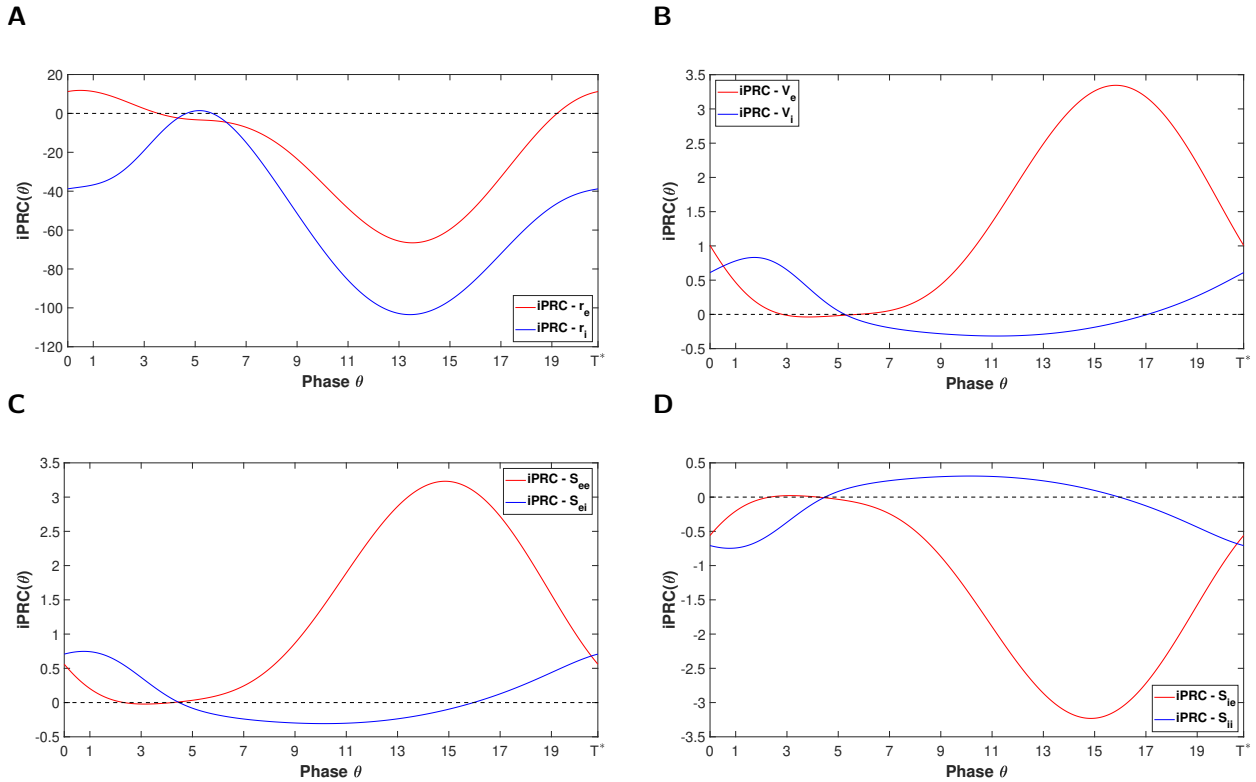

Figure 9: Infinitesimal phase response curves for the PING case: (**A**) firing rate variables, (**B**) mean membrane potential variables, (**C**) excitatory synapses and (**D**) inhibitory synapses. Red lines denote excitatory variables while blue lines denote the inhibitory ones. Parameters are as in (12). Period of limit cycle: $T^* = 20.811$ ms.

The $iPRC_{r_e}$ and $iPRC_{r_i}$ are mostly negative (Figure 9A), meaning that if we apply a small perturbation either to r_e or r_i, it will cause a delay in the phase or, in other words, the oscillator slows down. In Figure 9B) we observe the opposite situation. A perturbation in the V_e or V_i direction mostly advances the phase of the oscillator and thus speeds up its dynamics. Regarding the excitatory and inhibitory synapses (Figures 9C and 9D, respectively), a perturbation acting on the excitatory ones has an identical effect as for

the mean voltage (Figure 9B), while for the inhibitory synapses, the effect is symmetric to the excitatory ones with respect to the x-axis. That is, a perturbation in the direction of the inhibitory synapses, in general, delays the phase while in the direction of the excitatory ones, it advances the phase (with the same magnitude).

Recall that the magnitude of the iPRC measures how strong is the impact of a stimulus on the phase of an oscillator. In Figure 9, the $iPRC_{r_e}$ and $iPRC_{r_i}$ take large (negative) values, and this does not happen for the $iPRC_{V_e}$ and $iPRC_{V_i}$. The same stimulus applied to different variables causes therefore phase shifts of different magnitude.

We display the phase response curves for the ING setting in Figure 10. Both the PING and ING mechanisms share a common feature for their iPRCs; in almost all the phases of the oscillator an infinitesimally small perturbation on the r_e or r_i direction has a great impact by delaying the phase. On the other hand, the magnitude of the maximum (in absolute value) of the functions $iPRC_{V_e,V_i}$, $iPRC_{S_{ee},S_{ei}}$ and $iPRC_{S_{ie},S_{ii}}$ is small (see panels (**B**), (**C**) and (**D**) in Figures 9 and 10), meaning that the phase change is small.

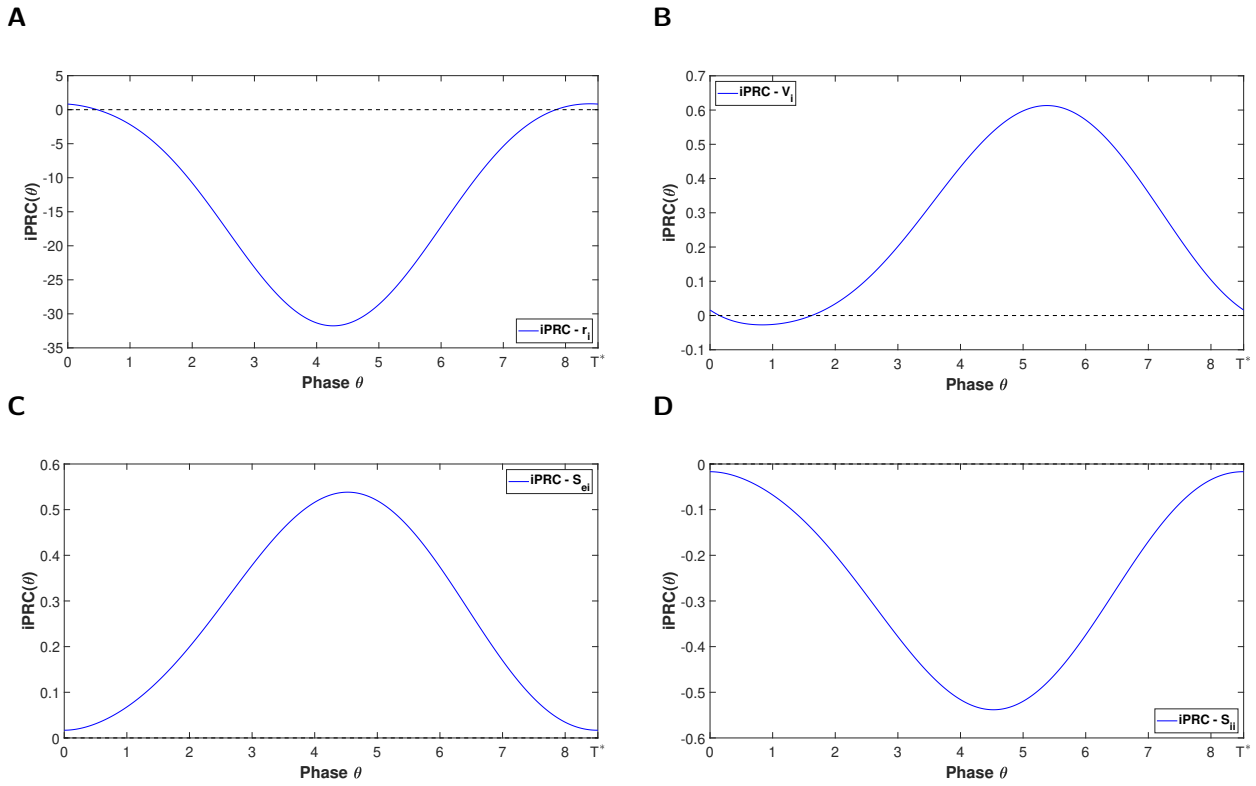

Figure 10: Infinitesimal phase response curve for the ING setting. (**A**) firing rate variable, (**B**) mean membrane potential variable, (**C**), inhibitory-to-excitatory synapse and (**D**) inhibitory-to-inhibitory synapse. Parameters are as in (13). Period of limit cycle: $T^* = 8.522$ ms.

3.3 Phase dynamics

In the previous section the oscillator was perturbed by a single and brief external pulse. In this section we perturb it by a continuous periodic function acting on one variable. As we shall see, the infinitesimal PRC will appear in the description of the phase dynamics of the forced oscillator.

We assume the same hypothesis presented at the beginning of Section 3.2. Consider the perturbed system $x = F(x) + A\,p(t)\,\vec{v}$, where $p(t)$ is a T-periodic perturbation and $\vec{v} = \vec{e}_2$, that is, in the direction of the excitatory mean potential variable, V_e. In the numerical simulations performed in this section, we apply a non-negative perturbation of the form $p(t) = 1 + \cos(\frac{2\pi t}{T})$, as in [11].

When the perturbation is applied, the periodic orbit Γ is slightly deformed and, the phase dynamics is modified in the following way:

$$\begin{aligned}\frac{d\theta}{dt} = \nabla\Theta(x(t)) \cdot \frac{dx}{dt} &= \nabla\Theta(x(t)) \cdot \Big[F(x(t)) + Ap(t)\,\vec{v}\Big] \\ &= \nabla\Theta(x(t)) \cdot F(x(t)) + A\nabla\Theta(x(t)) \cdot p(t)\,\vec{v} \\ &= 1 + A\,\nabla\Theta(x(t)) \cdot p(t)\,\vec{v}\,.\end{aligned} \tag{21}$$

Notice that now $x(t)$ refers to the perturbed solution and not the periodic orbit $\gamma(t)$ itself. On the periodic orbit $\gamma(t)$, the following equality is always true: $\dot{\theta} = \nabla\Theta(\gamma(t)) \cdot F(\gamma(t)) = 1$ (straightforward from the equation (15) and the definition of phase function $\Theta(x)$). However, we highlight that $\nabla\Theta(x(t)) \cdot F(x(t)) = 1$ is also true on any solution $x(t)$ (and not only on the limit cycle) because the phase function is not only defined for points on $\gamma(t)$ but also for those in the basin of attraction of the limit cycle. Notice $\nabla\Theta(x(t))$, does not correspond to the infinitesimal PRC of the previous section, as the latter was derived for points belonging to the periodic orbit, i.e. $Z(\theta) = \nabla\Theta(\gamma(\theta))$. That said, if the stimulus is weak enough so that $x(t)$ is assumed to be close to $\gamma(t)$ then we can approximate $\nabla\Theta(x(t))$ by $Z(\theta)$. By doing so, it is clear that the phase dynamics of the oscillator, when stimulated by an arbitrarily small-amplitude general perturbation $A\,p(t)$, is modified by adding the linear response of the oscillator to that stimulus. Then, at first order, it suffices to know the infinitesimal PRC in order to quantify the new phase dynamics. The assumption $\nabla\Theta(x(t)) \approx Z(\theta)$ is quite strong as we are claiming that, after stimulus, we still remain on the limit cycle but with different phase dynamics. This assumption is referred to as the *weak coupling hypothesis*.

3.3.1 Stroboscopic map and rotation number

Since $p(t)$ is periodic, we use the so-called *stroboscopic map* to study system (21). Let $\Phi_t(\theta)$ be the flow of the differential equation (21) starting at phase θ. The stroboscopic map is defined as the flow after a period of the external perturbation

$$\theta_{n+1} = P(\theta_n) = \Phi_T(\theta_n) \mod T^*\,. \tag{22}$$

Then, the behaviour of forced single oscillators can be accounted for the dynamics of the stroboscopic map (22). Fixed points of the stroboscopic map, i.e. $\theta = P(\theta)$, or periodic points, i.e. $\theta = P^m(\theta)$ for some $m \in \mathbb{N}$, correspond to periodic orbits of the forced system that provide information on phase-locking states.

We say that two oscillators are in $p : q$ *phase-locking* state if every time the first oscillator completes p revolutions the second one completes q. The most simple and well-known phase-locking is synchronization,

corresponding to a $1:1$ relation, that is, the oscillator makes a revolution for every cycle of the perturbation. This is the case of the example given in Figure 11. Initially, the oscillator completes a cycle after time T^* while the external forcing does so in a different time T. Eventually, the neural oscillator, stimulated externally by the T-periodic function, synchronizes with that forcing (i.e. they become in-phase).

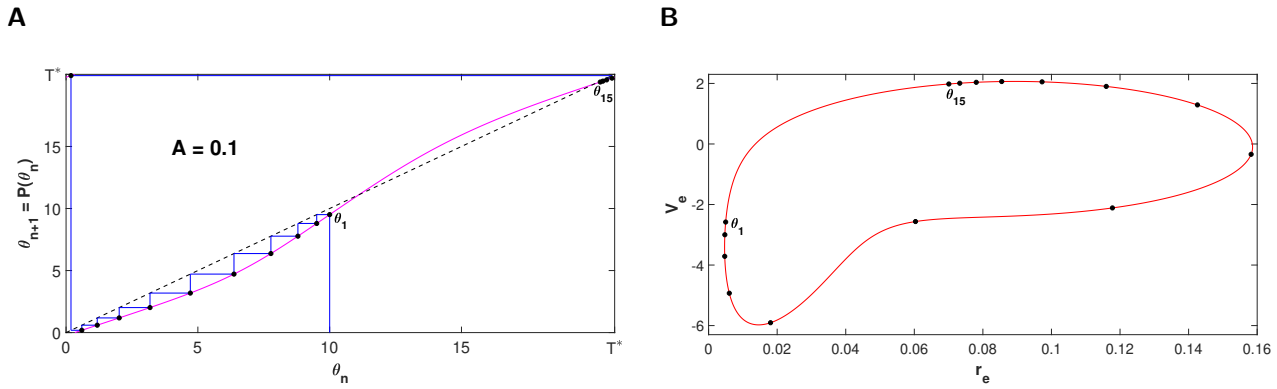

Figure 11: Synchronization between the oscillator and the perturbation. (**A**) Cobweb associated to the stroboscopic map (22) (purple line) with two fixed points: one stable and another unstable (topmost and bottommost intersection between the black-dashed diagonal and the purple-solid line, respectively). We start with an arbitrary phase θ_1, whose orbit (set of black-filled points) approaches to the stable phase. (**B**) Distribution of the orbit of θ_1 along the limit cycle of the unperturbed system (8) - (9) (recall we are assuming weak coupling hypothesis). Relation between oscillator's period and forcing period: $T = 0.87\,T^*$. Amplitude $A = 0.1$.

The $1:1$ phase-locking states correspond to fixed points of (22) because, after integrating a period of T (the forcing will have finished a revolution by that time), the final phase coincides with the initial one plus the natural period T^* (i.e. $\theta + T^* = P(\theta)$), that is, the orbit has closed. The relation $p:1$, consisting in p revolutions per one of the stimulus, also falls into this synchronization category and is thus a fixed point of the stroboscopic map (for such a relation we must find a fixed point of $\theta + pT^* = P(\theta)$); in time T the orbit has made p cycles per one of the forcing.

In the same way, the $1:2$ phase-locking means that per one cycle completed by the oscillator the forcing has completed two. This type of locking between the oscillator and the forcing is a 2-periodic point of equation (22), that is, a point that after two iterates comes back again to the starting point, i.e. $\theta + T^* = P^2(\theta)$. For the general case, the $1:q$ phase-locking is a q-periodic point of the stroboscopic map, i.e. $\theta + T^* = P^q(\theta)$.

Finally, in the most general framework, a $p:q$ phase-locking satisfies $qT - pT^* = 0$ (typically, this is called a resonant relation), indicating q oscillations of the forcing per p cycles of the orbit. That is,

$$\frac{T}{T^*} = \frac{p}{q} = \frac{\text{oscillator revolutions}}{\text{forcing revolutions}}\,. \tag{23}$$

The way of computing such phase-locked states is to find points θ satisfying $\theta + pT^* = P^q(\theta)$ for any $p, q \in \mathbb{N}^+$ (in doing so, we are actually seeking for periodic points of (22) but they are nothing else than fixed points of the composition of P up to some power).

The existence of such periodic points is given by a very well known result in the context of the circle maps. Let $f : \mathbb{S}^1 \to \mathbb{S}^1$ be a map on the circle, the *lift* of f is a continuous function $\overline{f} : \mathbb{R} \to \mathbb{R}$ that satisfies $\pi(\overline{f}(x)) = f(\pi(x))$, where $\pi(x) = x \bmod 1$ (i.e. the phase of the circle). Then, the *rotation number* of a map $f : \mathbb{S}^1 \to \mathbb{S}^1$ is given by

$$\rho(f) = \lim_{n\to\infty} \frac{\overline{f}^n(x) - x}{n}, \tag{24}$$

for any $x \in \mathbb{S}^1$. There are two important results to characterize the dynamics using the rotation number.

Proposition 3.1. *A diffeomorphism $f : \mathbb{S}^1 \to \mathbb{S}^1$ has periodic points if and only if its rotation number is rational.*

Theorem 3.2. *Let $f : \mathbb{S}^1 \to \mathbb{S}^1$ be an orientation-preserving diffeomorphism of class C^2 with irrational rotation number, $\rho(f) \in \mathbb{R}\backslash\mathbb{Q}$. Then, f is topologically conjugated to the irrational rotation of angle $\rho(f)$.*

These statements are interpreted as follows. If ρ is rational, then there exists a q-periodic point of the stroboscopic map (22), that is, a solution of $P^q(\theta) = \theta \mod T^*$. If, by contrast, ρ is irrational, then the orbits of (22) fill densely the circle.

We will compute the rotation number for the map (22). The procedure that we will use is presented in [14] and we summarize it here. First of all, notice that the definition (24) does not depend on the initial phase θ_0. We start with $\theta_0 = 0$ and iterate the stroboscopic map (22) N times (in practice $N = 350$ iterations have been conducted). We sort the phases $\{\theta_n\}_{n=1}^N$ in an increasing way. Let i and j be any two consecutive indexes and n_i and n_j the number of completed revolutions since start of phases θ_i and θ_j, respectively. Then, for any such a pair, we define ρ^{ij}_{min} and ρ^{ij}_{max} as follows:

- If $i < j$, then $\rho \geq \dfrac{n_j - n_i}{j - i} = \rho^{ij}_{\text{min}}$.
- If $i > j$, then $\rho \leq \dfrac{n_i - n_j}{i - j} = \rho^{ij}_{\text{max}}$.

We take the maximum (resp. the minimum) of the set of ρ^{ij}_{min} (resp. ρ^{ij}_{max}). The error by approximating the rotation number ρ either by $\rho_{\text{min}} := \max(\rho^{ij}_{\text{min}})$ or by $\rho_{\text{max}} := \min(\rho^{ij}_{\text{max}})$ is of order $1/N^2$ (for $N = 350$, $1/N^2 < 10^{-5}$).

Under this approach, we proceed to compute the rotation number of the stroboscopic map (22) for $T/T^* \leq 1$. These intervals in $(0, 1]$ where the graph of ρ takes the rational value p/q correspond to $p : q$ phase-lockings. The length of such regions depends on the forcing amplitude A; the smaller it is, the shorter the $p : q$ phase-locking interval. The rotation number has a fractal structure consisting of an infinite number of constant plateaus that is continuous everywhere. Because of that inherent structure, the graph of the rotation number is often called *Devil's staircase*. Among all these plateaus, the easiest detectable phase-lockings, for small amplitude, are those with a total number of cycles $p + q$ small so, for $T/T^* \in (0, 1]$, we expect to identify at least the synchronized state and maybe a $1 : 2$ phase-locking by observing two plateaus in the graph of ρ at heights 1 and $1/2$, respectively.

In Figure 12 we show the rotation number for different amplitudes A for the PING interplay perturbing the macroscopic variable V_e (i.e. in the direction $\vec{v} = \vec{e}_2$). Starting with the lowest amplitude, $A = 0.02$ (dark blue curve), we observe only one small plateau for periods T similar to the natural one T^* (i.e.

$T/T^* \approx 0.95$) where ρ is 1. Thus, at low amplitudes the oscillator synchronizes with external forcings at similar frequencies. Increasing the amplitude results in a lengthening of the $1:1$ plateau as well as the appearance of $1:1$ synchronization for even lower periods T (see, for instance, the red curve). At amplitude $A = 0.06$ a (very) small plateau at height $1/2$ becomes visible around $T/T^* \approx 0.45$, corresponding to the $1:2$ phase-locking (one revolution per two of the stimulus). As the amplitude increases, such a plateau grows while responding to increasingly higher-frequency stimuli $p(t)$. We remark the appearance of other phase-locking relations at large amplitudes; we detect a $2:3$, $3:2$ phase-lockings (plateaus of red and orange curves at heights $2/3$ and $3/2$, respectively) and even a $2:1$ relation for amplitude $A = 2$.

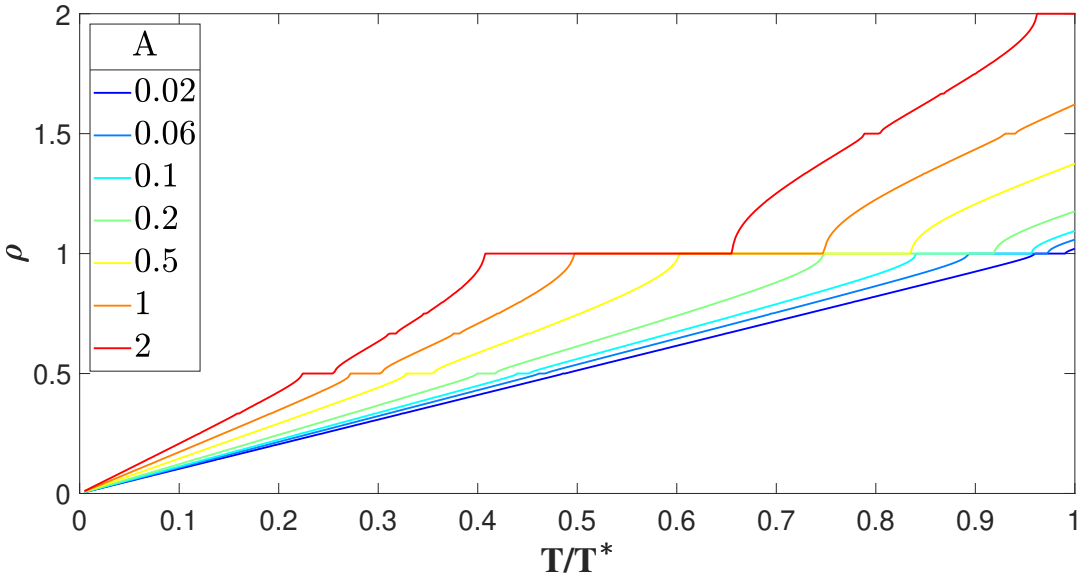

Figure 12: Rotation numbers (or Devil's staircases) associated to the stroboscopic map (22) for the PING mechanism with external periodic stimulus $A\,p(t)$ applied on the macroscopic variable V_e. At low amplitudes (cold color curves) a plateau at height 1 (i.e. a $1:1$ phase-locking) emerges and enlarges as the amplitude is increased (warm color curves). Other important frequency relations have become visible such as the $1:2$, $2:3$, $3:2$ and $2:1$ phase-lockings. The external perturbation is of the form $p(t) = 1 + \cos\left(\frac{2\pi t}{T}\right)$.

Another biologically meaningful approach is to perturb the mean inhibitory voltage V_i (i.e. in the direction $\vec{v} = \vec{e}_6$) of the PING mechanism. In Figure 13 we show the Devil's staircases associated to that case. As before, we observe a $1:1$ plateau for external periods T close to the natural one T^* that widens lightly as the amplitude rises. Apart from the synchronization plateau, from amplitude $A = 0.5$ onwards we detect clearly a $1:2$ frequency relation centered initially at $T/T^* \approx 1/2$. Unlike the PING case varying the variable V_e, the $p:q$ phase-lockings for this case have a tendency to take place for external perturbations $A\,p(t)$ with lower frequency. This fact may be noticed, for instance, comparing the displacement to the right of the plateaus for $A = 1$ and $A = 2$ (orange and red curves). We point out the existence of other phase-locked states at amplitude $A = 2$, such as the pair $1:3$ and $2:3$ (largest plateaus before and after the plateau $1/2$) as well as the $1:4$ and $3:4$ (at heights $1/4$ and $3/4$, respectively).

These Devil's staircases for the PING mechanism show that at large amplitudes, perturbing V_e entails

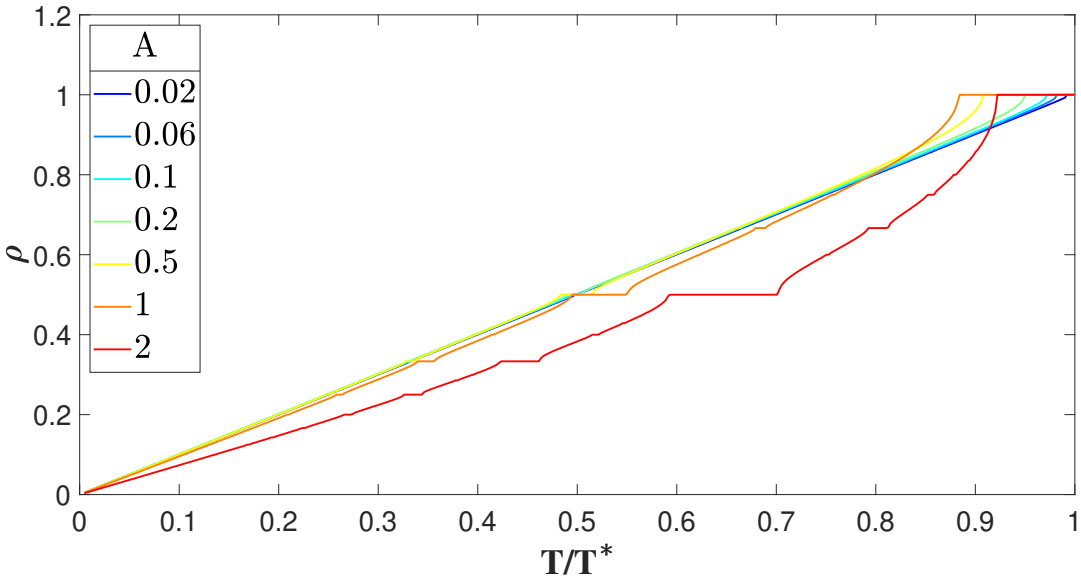

Figure 13: Rotation numbers (or Devil's staircases) associated to the stroboscopic map (22) for the PING mechanism with external periodic stimulus $p(t)$ applied on the macroscopic variable V_i. At low amplitudes (cold color curves) a plateau at height 1 (i.e. a $1:1$ phase-locking) emerges close to $T/T^* \approx 1$ and enlarges slightly as the amplitude is incremented (warm color curves). Similar for the $1:2$ phase-locking. Notice the certain tendency of the Devil's staircases to respond to lower frequency forcings (in comparison to the initial forcing period $T = pqT^*$). Other noticeable frequency relations are the pair $1:3$ and $2:3$ together with the $1:4$ and $3:4$. The external perturbation is of the form $p(t) = 1 + \cos\left(\frac{2\pi t}{T}\right)$.

synchronization at high frequencies while perturbing V_i at low ones. We will provide an interpretation of this fact in the next section.

We proceed analogously for the ING mechanism perturbing V_i. Figure 14 displays the Devil's staircases for the same set of amplitudes as before. We observe common characteristics with those in Figures 12 and 13. A subtle plateau at height 1 shows up at low amplitudes (blue curves) and becomes larger with some bias to the left (as in Figure 12). There appears also a $1:2$ plateau with a much smaller width than those emerged for the PING cases. No other plateaus are visible (at least for this set of amplitudes).

3.4 Arnold tongues

In the previous section, we have seen that the rotation number allows us to detect the values T/T^* for which the $p:q$ phase-lockings emerge. Furthermore, we have seen that these regions grow as the amplitude increases, and shrink until collapsing to a point as the amplitude decreases. In a (T, A) diagram, a $p:q$ phase-locking region resembles a leaf or a fang, known as *Arnold tongue*. The shape of such regions has been illustrated in Figure 15. Notice also that the plateaus in the graph of the rotation number correspond to slices of the Arnold tongues obtained by fixing the amplitude (see red line in Figure 15).

There is a strong relation between the PRCs and the shape of the Arnold tongues. If the PRC is mainly

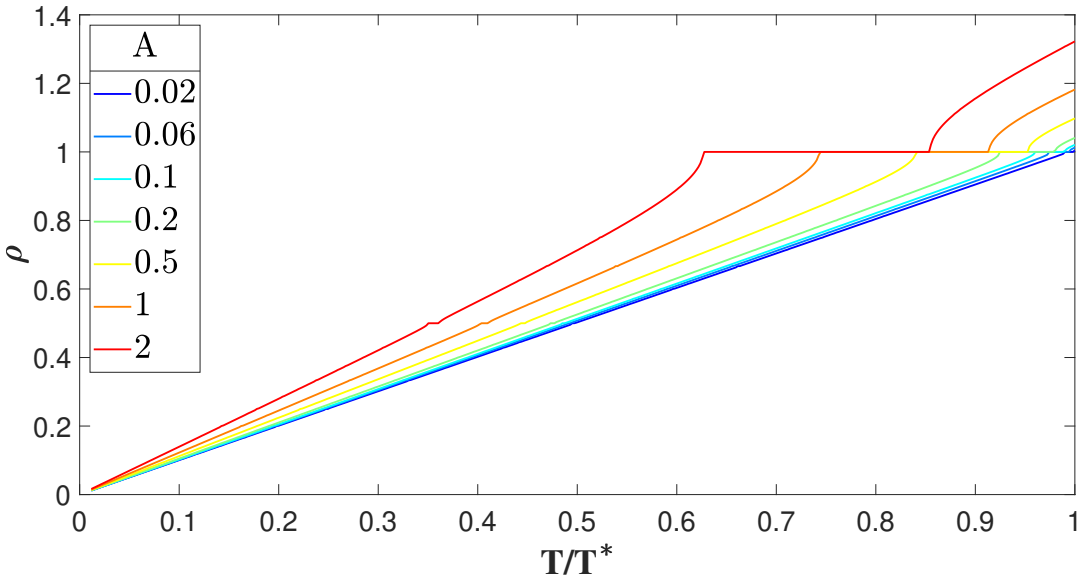

Figure 14: Rotation numbers (or Devil's staircases) associated to the stroboscopic map (22) for the ING mechanism with external periodic stimulus $p(t)$ applied on the macroscopic variable V_i. At low amplitudes (cold color curves) a small plateau at height 1 (i.e. a $1:1$ phase-locking) emerges close to $T/T^* \approx 1$ and becomes larger as the amplitude is incremented (warm color curves). A $1:2$ phase-locking starts to show up for large amplitudes (red and orange curves). As in Figure 12 we note some bias towards to faster stimuli $p(t)$. No other noticeable frequency relations are detected. The external perturbation is of the form $p(t) = 1 + \cos\left(\frac{2\pi t}{T}\right)$.

positive (e.g. the $iPRC_{V_e}$ for PING oscillations in Figure 9), the oscillator can essentially only advance its phase and thus it synchronizes almost exclusively to fast external oscillations, that is, periodic forcing with period $T < T^*$. The Arnold tongue for this case bends to the left (see left panel in Figure 15). This fact justifies why the $p:q$ phase-locking plateaus in Figure 12 shift gradually to the left (see, for instance, at the $1:1$ phase-locked state for different amplitudes). Analogously, when the PRC is mainly negative the Arnold tongue bends to the right and the oscillator mainly synchronizes to low frequency oscillations (as illustrated in the right panel in Figure 15).

The boundaries of the Arnold tongues correspond to the locus of a widely-known and ubiquitous bifurcation in Dynamical Systems: the saddle-node bifurcation. A saddle-node bifurcation is a qualitative change in the phase portrait that occurs when two fixed points, a saddle and a node, coalesce and disappear. As shown in Figure 16, for a fixed amplitude $A = 0.5$, outside of the $1:1$ Arnold tongue there are no fixed points (panel (**A**)), whereas within the Arnold tongue (panel (**B**)) there are two fixed points (one stable and another unstable) of the stroboscopic map (22). Such fixed points are born in one boundary of the Arnold tongue and annihilate each other in the opposite one.

These saddle-node loci can be (numerically) computed by identifying points (θ, T, A) such that the following two conditions hold:

— Fixed point condition: $P(\theta) - \theta = 0$

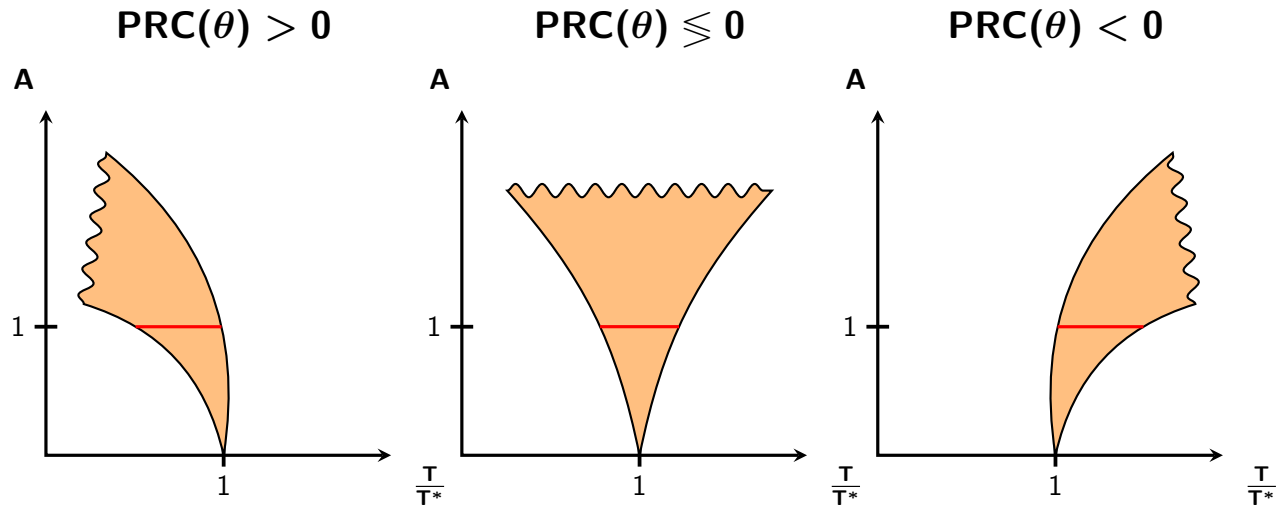

Figure 15: Schematic illustration of the relationship between a $1:1$ Arnold tongue and the main sign of the infinitesimal phase response curve. (Left panel & Right panel) If the PRC is predominantly positive (resp. negative), the Arnold tongue has a certain tendency to lean to the left (resp. right). (Middle panel) When the PRC is both positive and negative, the Arnold tongue is centered around $T/T^* = 1$. The red line is meant to clarify the relation between the rotation number and the corresponding Arnold tongue. Such a line would correspond to a $1:1$ plateau observed in the rotation number graphs.

— Saddle-node condition: $\frac{\partial P}{\partial \theta} - 1 = 0$

We will use these conditions to compute the saddle-node curve using a continuation method. The continuation method is a numerical procedure by which one can find solutions of an implicit parametrized function $G(\mathbf{u}, \lambda) = 0$, with $\mathbf{u}$ the set of variables and λ a real parameter. In this project we implement the *Conditioned Extrema Method* that combines a tangent-like approximation as in the Keller's (pseudo-arclength) method and a modified Newton method (based on a minimization problem with a restriction) to refine it. Starting from an initial solution $(\mathbf{u_0}, \lambda_0)$ lying on the curve $G(\mathbf{u}, \lambda) = 0$, the method consists in making a prediction for the next point on the continuation curve by moving along the tangent line at the point $(\mathbf{u_0}, \lambda_0)$. Then, we correct the approximate point successively by means of a modified Newton method. Since, the number of variables is higher than the number of equations in the equation $G(\mathbf{u}, \lambda) = 0$, we need to impose the additional condition that the norm of the correction must be a minimum. We solve this problem using Lagrange multipliers. We present the method in great detail for a general setting in Appendix B.

In our case, we have only one variable θ, and two parameters, T and A, and we want to pinpoint the boundary of any Arnold tongue, using the two conditions described above. Therefore, we are under the hypotheses of the Conditioned Extrema Method: three variables (θ plus parameters T and A, after allowing them to evolve according to $\dot{T} = \dot{A} = 0$) and two equations (fixed point and saddle-node conditions). Let $w = (\theta, T, A)$ be the unknowns and $\widetilde{\Phi}_t(\theta, T, A)$ be the extended flow associated to the phase equation (21) when T and A are treated as variables. Let $\widetilde{P}$ be the stroboscopic map resulting from that extended flow, that is,

$$\widetilde{P}(\theta, T, A) := \widetilde{\Phi}_T(\theta, T, A) \mod T^* . \tag{25}$$

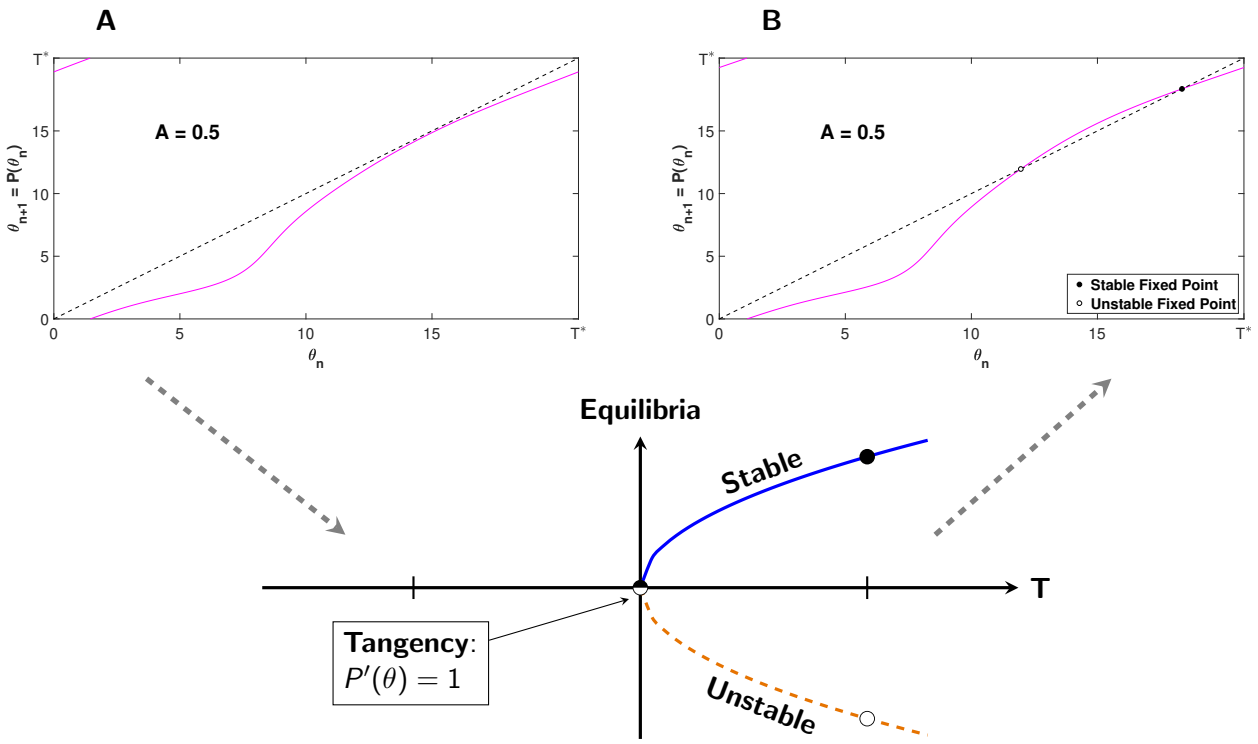

Figure 16: Example of a saddle-node bifurcation on the stroboscopic map (22). (**A**-**B**) Graph of the stroboscopic map P - purple solid line - before and after a saddle-node bifurcation. (**A**) The stroboscopic map has no fixed points as it does not intersect the line $y = x$ (black-dashed line). (**B**) The stroboscopic map does intersect the line $y = x$ in two fixed points: one stable (black-filled circle) and one unstable (white-filled circle). (Bottom panel) A classical saddle-node bifurcation diagram with respect to parameter T. On the left side of the diagram, the stroboscopic map does not intersect the black-dashed line $y = x$ while in the right one it does so in a stable (blue-solid line - black-filled circle) and an unstable (orange-dashed line - white-filled circle) fixed points. The bifurcation occurs at the values of the parameter for which there exists a tangency of the map (22) with the line $y = x$. Panels (**A**-**B**): PING mechanism with external perturbation $p(t)$ applied on the variable V_e with $A = 0.5$ and a period relation of (**A**) $T = 0.6\,T^*$ and (**B**) $T = 0.61\,T^*$ (see Devil's staircases in Figure 12).

Notice that Φ_t is the flow of (21) (with stroboscopic map $P(\theta)$) while $\widetilde{\Phi}_t$ is the extended one (with stroboscopic map $\widetilde{P}(\theta, T, A)$). Therefore, we define $G(w)$ as the system of the following two nonlinear equations

$$G(w) = G(\theta, T, A) = \begin{pmatrix} \widetilde{P}(\theta, T, A) - \theta \\ \dfrac{\partial}{\partial\theta}(\widetilde{P}(\theta, T, A)) - 1 \end{pmatrix} = \begin{pmatrix} \widetilde{\Phi}_T(\theta, T, A) \bmod T^* - \theta \\ \dfrac{\partial\widetilde{\Phi}_T}{\partial\theta}(\theta, T, A) \bmod T^* - 1 \end{pmatrix}. \tag{26}$$

Recall that $G(w) = 0$ defines implicitly the boundary of the Arnold tongue. When the amplitude is zero and the forcing period satisfies a rational relation $T = \frac{p}{q}T^*$, then any phase θ is a $p : q$ phase-locking state of the forced oscillator. Consider, for instance, the case $T = T^*$ where we perturb an oscillator with a periodic function with the same period. It is clear that all the phases θ of the forced oscillator are in a $1 : 1$ relation with the external forcing. In the (T, A)-plane this corresponds to a point lying on the $1 : 1$ Arnold tongue's boundary and on $A = 0$. From this point, two saddle-node branches are born, delimiting the $1 : 1$ region for non-zero amplitudes (see panels in Figure 15).

To start the method we must provide a "good" (i.e. close) initial seed. One might consider the point at the intersection of both branches, but this does not serve as starting point since the tangent (42) is not well-defined. A typical strategy is to consider a point near the birth of the saddle-nodes curves. This means taking a nonzero small amplitude and a period T close to $\frac{p}{q}T^*$. For such values, the stroboscopic map (22) should intersect (at least) twice the $y = x$ line. Such points, which are solutions of the equation $P(\theta) - \theta = 0$, can be computed using any root-finding method. For that purpose, we have used a bisection method because of its simplicity and also because we do expect not so many iterations to converge. Any of those solutions, together with the chosen period and amplitude, form an initial seed (arbitrarily) close to the left or right boundary.

In the preceding section, we acquired significant qualitative and quantitative results on the shape of some $p : q$ Arnold tongues by means of the rotation number. Such results may give a much better initial seed for the left and right branches for nonzero amplitude. Indeed, if one observes, for instance, the PING mechanism perturbing the variable V_e (see Figure 12) with an amplitude $A = 0.2$, the $1 : 1$ plateau starts and ends around $T \approx 0.75T^*$ and $T \approx 0.9T^*$, respectively. Once we know these parameter values we proceed as before; we seek either of the two fixed points θ with a bisection method and we finally construct the initial conditions $w^{l,r}$ (one for the left boundary and the other for the right one). Once we have refined the initial seed we apply the continuation process.

There is a final issue that we have to take care of and this is the differential of the map G, required in the refinement of the approximate solution by the Netwon's method (see the iterative equation (49) in Appendix B). This requires a further study on variational equations that we present in Appendix C. Moreover we also present a method to compute the derivatives of a periodic function by means of Fast Fourier transform algorithms.

In Section 3.3 we linked a general $p : q$ phase-locking state with fixed/periodic points of the stroboscopic map (22). Thus far we have derived the expression for the $1 : 1$ Arnold tongue boundary (see Appendix C). If we are interested in the boundary of the Arnold tongues of the $p : 1$ phase-locking, $p \in \mathbb{N}$, we only have to consider the initial condition and proceed exactly with the same methodology described in Appendix C. Indeed, notice that when we defined the locus of an Arnold tongue boundary via equation (58) we took modulus T^*, so the first component of G does not distinguish between a fixed point of the equation $P(\theta) = \theta + T^*$ from one of $P(\theta) = \theta + pT^*$. That is why we only have to be concerned on

picking a good enough initial seed for the $p:1$ boundary.

This is no longer true when we seek for $1:q$ regions, which requires a slight modification in the definition of G and thus in the derivation of the matrix DG. The difference lies on the fact that we are not looking for a fixed point anymore but a periodic one. The Arnold tongue boundary is described by the equation $P^q(\theta) = \theta + T^*$ (we will omit T^* when doing modulus) and its partial derivative with respect to θ. Similar in spirit to the equations (26), the following system of nonlinear equations defines implicitly the boundary of the $1:q$ Arnold tongues

$$G(w) = G(\theta, T, A) = \begin{pmatrix} \widetilde{P}^q(\theta, T, A) - \theta \\ \dfrac{\partial}{\partial\theta}\left(\widetilde{P}^q(\theta, T, A)\right) - 1 \end{pmatrix} = \begin{pmatrix} \widetilde{\Phi}_{qT}(\theta, T, A) - \theta \\ \dfrac{\partial\widetilde{\Phi}_{qT}}{\partial\theta}(\theta, T, A) - 1 \end{pmatrix}, \tag{27}$$

where we have applied the transitivity property of a flow: $\widetilde{\Phi}_T(\widetilde{\Phi}_S(\theta, T, A), T, A) = \widetilde{\Phi}_{T+S}(\theta, T, A)$. Notice that now the extended flow $\widetilde{\Phi}_t$ is integrated up to a larger time qT. This is the only difference between the $1:1$ and $1:q$ Arnold tongues. The corresponding differential matrix DG is derived in Appendix C.

We now present the most noticeable Arnold tongues computed using the continuation method described above for the three cases that we have been considering so far: the PING mechanism perturbing either in the V_e or V_i direction, and ING mechanism perturbing in the V_i-direction.

For the PING mechanism, if the perturbation acts on the variable V_e the largest Arnold tongues correspond to the $1:1$, $1:2$ and $2:1$ phase-locking states (see Figure 17). As expected, the three Arnold tongues bend gradually to the left as the amplitude increases (as shown in Figure 12). It seems that for low-frequency perturbations (i.e. $T/T^* \geq 1$) the resulting Arnold tongues bend more sharply than for high-frequency perturbations (compare how the $1:2$ phase-locking bends in comparison with the $2:1$ phase-locking).

For the PING mechanism applying the perturbation to the variable V_i, there arise other significant Arnold tongues such as the $1:3$ and $2:3$. In Figure 18 we illustrate the four most perceptible Arnold tongues: the $1:1$, $1:2$, $1:3$ and $2:3$. As suggested by Figure 13, the Arnold tongues are initially centered around its corresponding period relation $\frac{T}{T^*} = \frac{p}{q}$ for relatively small amplitudes. As the amplitude increases the phase-locking states occur for periods T larger than their corresponding $\frac{p}{q}T^*$. We remark that the synchronized state (orange Arnold tongue) is much wider than the other coherent states, meaning that synchronization between oscillators may be achieved for a broader range of values (T, A).

Finally, we present the results for the ING mechanism with a perturbation acting on the V_i-direction (Figure 19). We draw similar conclusions as those obtained for the PING mechanism in Figure 17: the most significant Arnold tongues deviate slightly to the left. We also note that, for this case, the phase-locking states are narrower than those presented in Figure 17.

Remark: To find an good initial seed for the $2:1$ Arnold tongues in Figures 17 and 19 as well as the $1:1$ Arnold tongue in Figure 18, we had to compute the rotation number for amplitude $A = 2$ for a larger period relation (i.e. $T/T^* \geq 1$), so that we could capture properly the boundaries of such tongues (results not shown).

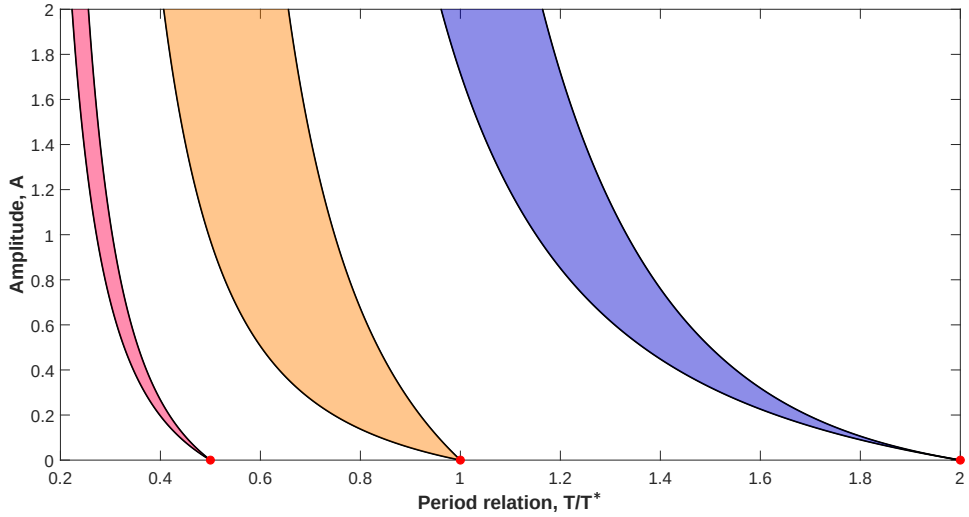

Figure 17: Arnold tongues corresponding to the most relevant phase-locking states for the PING mechanism with perturbation in the V_e-direction. Color legend of Arnold tongues: $1:1$ phase-locking (orange), $1:2$ phase-locking (purple) and $2:1$ phase-locking (blue). Red circles indicate the points where these Arnold tongues are born (at $T = \frac{p}{q}T^*$ for the corresponding $p, q \in \mathbb{N}$). Note that the Arnold tongues bend progressively to high-frequency perturbations (i.e. $T/T^* \leq 1$).

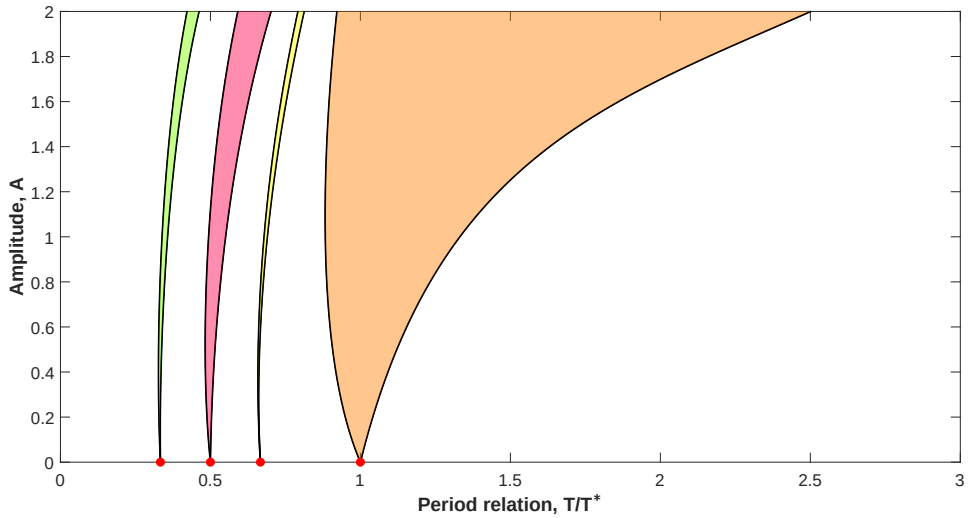

Figure 18: Arnold tongues corresponding to the most relevant phase-locking states for the PING mechanism with perturbation in the V_i-direction. Color legend of Arnold tongues: $1:1$ phase-locking (orange), $1:2$ phase-locking (purple), $1:3$ phase-locking (green) and $2:3$ phase-locking (yellow). Red circles indicate the points where these Arnold tongues are born (at $T = \frac{p}{q}T^*$ for the corresponding $p, q \in \mathbb{N}$). Note that the Arnold tongues are centered around $T = \frac{p}{q}T^*$ for small amplitudes and they are bent to low-frequency perturbations for large amplitudes.

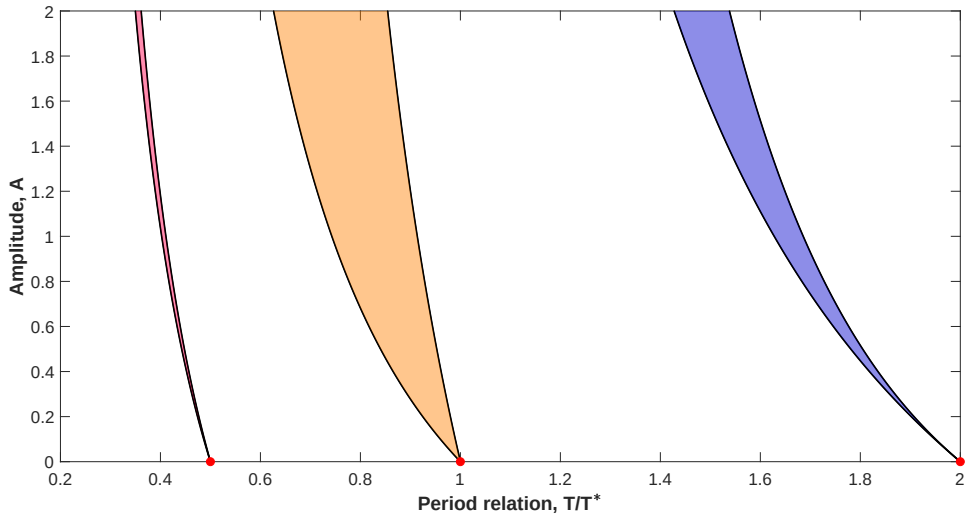

Figure 19: Arnold tongues corresponding to the most relevant phase-locking states for the ING mechanism with perturbation in the V_i-direction. Color legend of Arnold tongues: $1:1$ phase-locking (orange), $1:2$ phase-locking (purple) and $2:1$ phase-locking (blue). Red circles indicate the points where these Arnold tongues are born (at $T = \frac{p}{q}T^*$ for the corresponding $p, q \in \mathbb{N}$). Note that the Arnold tongues are bent to high-frequency perturbations.

4. Implications for CTC

In this section we present a first approach to the biological interpretation of the phase-locking states of Section 3.4. In particular, we will focus on the implications of the synchronized states to the communication through coherence (CTC) theory following [11]. Along this section we consider the synchronized state emerging for the PING mechanism when the network receives an input to the E cells (see Figure 17).

The CTC theory proposes that neural communication between two populations is more effective when the underlying oscillations are phase-locked. In our excitation-inhibition system, an external input may be ignored depending on whether the inhibition is present or not. If the external input reaches the receiving population before the inhibition activates, then it may contribute to increasing the activity of the excitatory receiving population and thus, promoting effective communication. On the other hand, if the input is received when the inhibition is present, then such a stimulus may not have any effect on the excitatory population. Hence, the effective communication depends essentially on the timing of the the inhibition and the external input.

To study effective communication, we define $\Delta\tau$ as the time difference between the maximum of the inhibition and the maximum of the external perturbation $p(t)$, that is,

$$\Delta\tau = \frac{t_{\text{inh}} - t_p}{T}\,, \tag{28}$$

where t_{inh} and t_p denote the times where the maximum of inhibition and of the sinusoidal perturbation $p(t)$ are achieved, respectively. If $\Delta\tau$ is positive then inhibition follows the input, which may allow a rise in the excitatory activity of the receiving population. By contrast, if $\Delta\tau$ is negative inhibition precedes the

input and the input may be ignored, bringing on an small effect onto the excitatory population (i.e. the population is less responsive to such a stimulus).

The magnitude of the effect of the perturbation onto the activity of the excitatory population can be measured as well. We thus define $\Delta\alpha$ as the ratio between the maximum excitatory activity with non-zero input, R_e^A, and the maximum excitatory activity with no external input, R_e^0, that is,

$$\Delta\alpha = \frac{R_e^A}{R_e^0}\,. \tag{29}$$

We expect that if $\Delta\alpha$ is larger than one, the input has an important effect onto the receiving population by increasing its activity, causing an effective communication. The external perturbation is a positive sinusoidal function, which means that it can only increase the activity of the receiving population (i.e. $\Delta\alpha \geq 1$).

To get a first intuition of the inhibition-perturbation timing and the effect of a perturbation in the $1:1$ Arnold tongue we consider three different points along such an Arnold tongue at a small amplitude. Recall that the whole study on the phase-locking states has been carried out under the restrictive weak coupling condition, which applies to small perturbations. With this we want to remark that the prediction for the phase reduction may fail on the $1:1$ Arnold tongue. We expect, nonetheless, that for small amplitudes the periodic orbit exists.

In Figure 20 we have picked three equidistributed points along the $1:1$ Arnold tongue at amplitude $A = 0.3$ (see x coloured marks in the left panel) and we have computed its corresponding perturbed limit cycles (discontinuous limit cycles in the right panel) projected onto the (r_e, V_e)-space. To find such perturbed orbits we have integrated the perturbed system forward in time for sufficiently large time. The perturbed system consists essentially of the same system (8) - (9) except that in the total excitatory input current I_e (equation (10)) we add the following term in red

$$I_e = I_e^{\text{ext}} + \tau_e S_{ee} - \tau_e S_{ei} + \tau_e A\, p(t)\,. \tag{30}$$

We note that the perturbed limit cycles have increased along the (r_e, V_e) directions compared with the original one (red-solid curve in right panel). It seems that the further is the point $(T/T^*, A)$ from $T/T^* = 1$, the bigger the periodic orbit gets. Recall that the period of such oscillations is actually the same as that of the external perturbation, T, that is slightly different in each one of the x-marks.

The factors $\Delta\tau$ and $\Delta\alpha$ have been measured for the three points in the left panel. We show the results in Table 1

	T/T^*	$\Delta\tau$	$\Delta\alpha$
Dark blue x-mark	0.7321	0.3147	3.3881
Cyan x-mark	0.7977	0.1965	2.7832
Green x-mark	0.8633	0.0860	1.9476

Table 1: Factors measuring the timing between the inhibition and the perturbation $\Delta\tau$ (equation (28)), and the effect of the perturbation onto the excitatory population $\Delta\alpha$ (equation (29)), for each of the three x-marks in Figure 20

In view of the results in Table 1, the first naive intuition is that, from the left boundary to the right, both factors $\Delta\tau$ and $\Delta\alpha$ decrease. We also observe that $\Delta\tau$ is positive (for these three points) and that

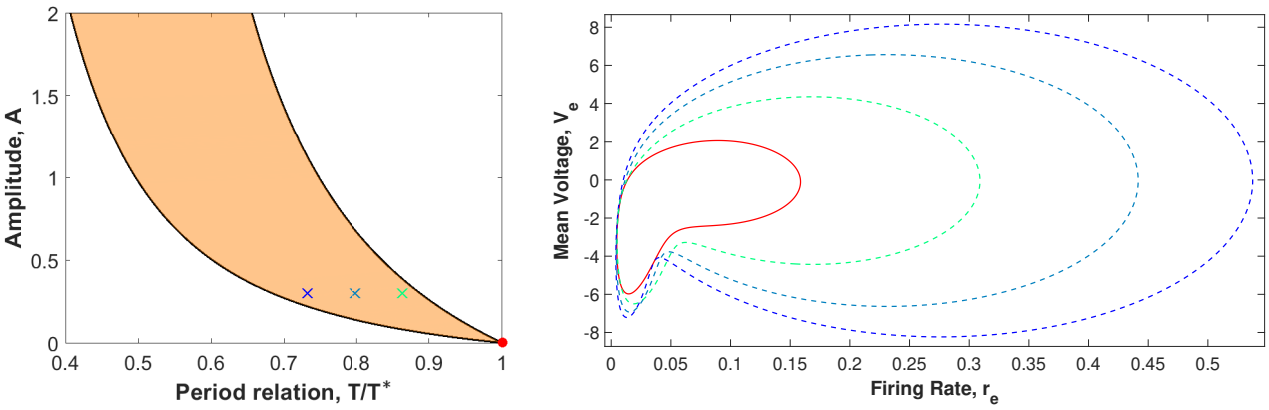

Figure 20: Existence of limit cycles for the perturbed system. (Left panel) Plot of the $1:1$ Arnold tongue for the PING mechanism (with external perturbation on V_e) with three equidistributed points. (Right panel) Limit cycles corresponding to the x-marks in the left panel (discontinuous curves). Period relation: $T \approx 0.7321\,T^*$ (dark blue x-mark), $T \approx 0.7977\,T^*$ (cyan x-mark) and $T \approx 0.8633\,T^*$ (green x-mark). Amplitude $A = 0.3$.

$\Delta\alpha$ is larger than 1. We conclude that the perturbation comes first than the inhibition in these three points, contributing to an increasing activity on the excitatory population. The phase difference between the inhibition and the perturbation seems to shorten as we lower the frequency of the external input $p(t)$. In Figure 21 we show the excitatory and inhibitory firing activity (red and blue, respectively) as well as the external perturbation $p(t)$ (green-dashed line) for the three x-marks (from (**A**) to (**C**), they correspond to the dark blue, the cyan and the green x-marks in Figure 20). We observe that initially inhibition follows the perturbation (panel (**A**)) and the phase difference between their maximum values (difference between blue and green points) is slightly reduced as we approach to the right boundary. We also remark that the effect of the perturbation has diminished as well.

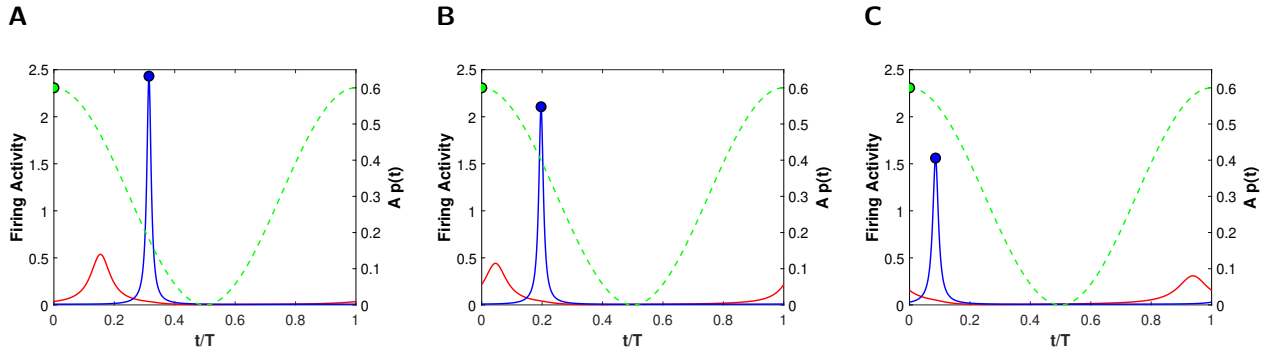

Figure 21: Firing activity and external perturbation for each one of the three x-marks introduced in Figure 20. Panels: (**A**) dark blue x-mark, (**B**) cyan x-mark and (**c**) green x-mark. Red and blue solid lines represent the excitatory and inhibitory firing activity. Green-dashed line represents the perturbation $p(t)$. Blue and green circles denote where the maximum of the inhibition and the maximum of the perturbation are reached.

5. Conclusions

In this project we have studied the coherent states that emerge when an oscillator is weakly periodically forced. To do so, we have used a semi-analytical expression of the phase response curve of the oscillator (solution of system (40), normalized by formula (41)) to reduce the study of the dynamics to the phase equation (21), describing the perturbed phase dynamics along the oscillator. We have computed the stroboscopic map and the rotation number to gain insight into both the width and the shape of the Arnold tongues (phase-locking states) in the $(T/T^*, A)$-plane: iPRC mainly positive means phase-locking with faster inputs, while iPRC mainly negative implies the opposite. Finally, we have used a continuation method to determine the most relevant (and largest) Arnold tongues. We point out that our study has been performed under a very strong condition, the weak coupling condition, that we comment next.

The weak coupling hypothesis is a double-edged sword. On one side, it provides a semi-analytical way to compute the infinitesimal phase response curve, which leads to the definition of the phase equation and its study. On the other, it limits the study to "weak" stimuli as we suppose that the perturbation has only modified the intrinsic phase dynamics of the perturbed orbit while keeping the same shape as the original one. Under external perturbations, the new dynamics could have changed drastically compared to the initial one (e.g. disappearance of the orbit for large amplitude, emergence of any other type of stable invariant object, etc), which makes the weak coupling assumption very restrictive. All the results we have obtained should be therefore contrasted with the full model.

In Section 4 we have provided a biological interpretation of the synchronized coherent state. We concluded that the inhibition-perturbation timing was positive and larger in the left boundary than in the right one of the 1:1 Arnold tongue. Close to the right boundary, it seemed that the effect of the perturbation decreased, making the receiving population less responsive to such perturbation. These conclusions should be revised carefully with a more accurate analysis of the factors $\Delta\tau$ and $\Delta\alpha$ defined in (28) and (29), respectively, along the whole $1:1$ Arnold tongue. This would entail also a study on the existence and/or disappearance of the perturbed limit cycle as a function of the period relation T/T^* and the amplitude A. We may also extend this study to other phase-locking states.

This project has based, essentially, on the work presented in [11] with two major differences. First, we have worked with a more realistic neural model (introduced in [2] and based on an exact model for the macroscopic description of neural networks in [8]), capturing many macroscopic states that the ad-hoc mean-field models fail to capture. Second, we have addressed the study of the emerging phase-locking patterns using a different methodology, that is, via the reduction to the phase equation. Unlike the classical 2-dimensional Wilson-Cowan model (used in [11]), the reduction to the phase equation (and the weak coupling condition) has simplified significantly the study of an 8-dimensional model, while obtaining similar results as those presented in [11] for small amplitudes.

This master dissertation has focused essentially on the study of the emerging phase-locking states under an external perturbation that it is not being affected by the oscillator. In doing so, the oscillator adapts to that of the external forcing, either speeding up (e.g. $1:1$ Arnold tongue in Figure 17) or slowing down (e.g. most of the $1:1$ Arnold tongue in Figure 18). However, this situation could no longer happen when we consider two (or more) mutually coupled oscillators (either identical or different) that interact with each other (as studied in [2]). In this case, both oscillators are constantly affected by the other oscillator. This type of problem could be tackled by means of the phase equation as well, except that now we should study a system of two coupled phase equations. It is an interesting project for future work.

6. Acknowledgements

Work produced with the support of a 2019 Leonardo Grant for Researchers and Cultural Creators, BBVA Foundation. The Foundation takes no responsibility for the opinions, statements and contents of this project, which are entirely the responsibility of its authors.

We acknowledge the use of the UPC Dynamical Systems group's cluster for research computing (see https://dynamicalsystems.upc.edu/en/computing/).

References

[1] G. Buzsáki and X-J. Wang. Mechanisms of gamma oscillations, *Annual Review of Neuroscience* **35** (2012), 203-225.

[2] G. Dumont and B. Gutkin. Macroscopic phase resetting-curves determine oscillatory coherence and signal transfer in inter-coupled neural circuits, *PLoS Computational Biology* **15 (5)** (2019), 1007019.

[3] B. Ermentrour and D. Terman. *Mathematical Foundations of Neuroscience*. New York: Springer-Verlag, 2010.

[4] J. Guckenheimer and P. Holmes. *Nonlinear Oscillations, Dynamical Systems, and Bifurcations of Vector Fields*. New York: Springer-Verlag, 1983.

[5] L. Hodgkin and F. Huxley. A quantitative description of membrane current and its application to conduction and excitation in nerve, *J. Physiol* **117** (1952), 500-544.

[6] E.M. Izhikevich. *Dynamical Systems in Neuroscience: The Geometry of Excitability and Bursting*. The MIT Press, 2007 (Chapter 10 can be found in the author's website https://www.izhikevich.org/publications/dsn/index.htm).

[7] E.M. Izhikevich. Which model to use for Cortical Spiking Neurons?, *IEEE Transactions on Neural Networks* **15 (5)** (2004), 1063-1070

[8] E. Montbrió, D. Pazó and A. Roxin. Macroscopic description for networks of spiking neurons, *Physical Review X* **5 (2)** (2015), 021028.

[9] V. Novičenko and K. Pyragas. Computation of phase response curves via direct method adapted to infinitesimal perturbations, *Nonlinear Dyn* **67** (2012), 517-526.

[10] F. Pascal. Rhythms for cognition: Communication through coherence, *Neuron* **88 (1)** (2015), 220-235.

[11] A Pérez-Cervera, T.S. Seara and G. Huguet. Phase-locked states in oscillating neural networks and their role in neural communication, *Commun Nonlinear Sci Numer Simulat* **80** (2020), 104992

[12] N.W. Schulthesis, A.A. Prinz and R.J. Butera. *Phase Response Curves in Neuroscience: Theory, Experiment, and Analysis*. New York: Springe-Verlag, 2012.

[13] C. Simó. On the analytical and numerical approximation of invariant manifolds, In *Modern Methods in Celestial Mechanics* (1990).

[14] C. Simó. Lecture notes of the PhD Course, "Numerical methods for Dynamical Systems" (2004).

[15] P.H. Tiesinga and T.J. Sejnowski. Mechanisms for phase shifting in cortical networks and their role in communication through coherence *Frontiers in Human Neuroscience* **196 (4)** (2010).

[16] H.R. Wilson and J.D. Cowan. Excitatory and inhibitory interactions in localized populations of model neurons *Biophysical Journal* **12 (1)** (1972), 1-24.

A. The Adjoint method for computing PRCs

Here we present a deduction of the adjoint method for a general setting (adapted from [3] and [12]).

Let us assume the hypothesis presented at the beginning of Section 3.2. Let $\varphi(t,x)=\varphi_t(x)$ be the flow associated to the differential equation $\dot{x}=F(x)$. The first variational equations along a solution $\varphi_t(x)$ quantify how is the linear behaviour around a solution $\varphi_t(x)$, for the solutions starting infinitesimally close to x. Mathematically, variational equations are formulated as the following Cauchy problem:

$$\begin{cases} \dfrac{d}{dt}\dfrac{\partial\varphi_t(x)}{\partial x} = D_xF(\varphi_t(x))\,\dfrac{\partial\varphi_t(x)}{\partial x}\,, \\ \dfrac{\partial\varphi_t(x)}{\partial x}\Big|_{t=0} = Id\,. \end{cases}$$

To solve the problem numerically, we will integrate it together with the original system, making a system of $n+n^2$ ODEs.

We consider now the first variational equations around the T^*-periodic solution $\gamma(t)$,

$$\frac{d}{dt}\psi(t) = A(t)\psi(t)\,, \tag{31}$$

where $A(t):=D_xF(\gamma(t))$. Since $\gamma(t)$ is T^*-periodic, system (31) has periodic coefficients. The previous equality can be expressed as a linear operator

$$(L\psi)(t) := \frac{d}{dt}\psi(t) - A(t)\psi(t) = 0\,. \tag{32}$$

The solution of a linear system with periodic coefficients is not, in general, periodic. However, the domain of definition of the solution ψ is compact and bounded since, because of the periodicity of $\gamma(t)$, it suffices to know the solution on $[0,T^*]$. It turns out that the operator is bounded and, because of the linearity, also continuous. Then, in the Hilbert space formed by the set of differentiable real-valued with bounded domain functions endowed with the usual inner product

$$(\psi,\phi) = \int_0^{T^*} \psi(s)\phi(s)ds\,, \tag{33}$$

there exists a unique adjoint linear operator L^* satisfying $(u,Lv)=(L^*u,v)$ where L^* is defined as

$$(L^*\phi)(t) := -\frac{d}{dt}\phi(t) - A(t)^T\phi(t)\,. \tag{34}$$

We check now that the infinitesimal PRC is a solution of the adjoint operator (34). On the way forward, we proceed similarly as when we introduced the infinitesimal PRC. We consider a solution on the limit cycle starting with phase ϕ_0, i.e. $x(t)=\gamma(t+\phi_0)$ (typically, the initial phase ϕ_0 is zero) and let $y(t)=x(t)+\varepsilon s(t)$ be a slight perturbation of $x(t)$ in such a way that $y(t)$ approaches the limit cycle. First, we note that the perturbation $s(t)$ satisfies the first variational equations (i.e. $(Ls)(t)=0$). Indeed, since $y(t)$ is a solution of $\dot{x}=F(x)$,

$$\frac{dx}{dt}+\varepsilon\frac{ds}{dt} = \frac{dy}{dt} = F(y(t)) = F(x(t)+\varepsilon s(t)) = F(x(t)) + \varepsilon DF(x(t))\cdot s(t) + \mathcal{O}(\varepsilon^2)\,. \tag{35}$$

Equating the coefficients of order ε, we reach that $s(t)$ is a solution of the linearized system

$$\frac{ds}{dt} = DF(x(t)) \cdot s(t)\,. \tag{36}$$

A Taylor expansion of the phase map $\Theta(y(t))$ about the solution on the limit cycle reveals the expression of the PRC at first order as the product of the phase variation times the perturbation (see equation 18), that is,

$$\Theta(y(t)) - \Theta(x(t)) = \varepsilon \nabla\Theta(x(t)) \cdot s(t) = \varepsilon Z(t) \cdot s(t)\,. \tag{37}$$

Generally, at time t, the perturbed solution $y(t)$ will be associated to an asymptotic phase that, initially, could be different from that of $x(t)$ (i.e. solutions $x(t)$ and $y(t)$ at time t lie in different isochrons). Nonetheless, by definition of isochrons, when these solutions evolve in time their phase difference will be maintained at all times and therefore the above relation does not depend on time. Following this argument we have that

$$\begin{aligned} 0 = \frac{d}{dt}\big(Z(t)\cdot s(t)\big) &= \frac{dZ}{dt}\cdot s(t) + Z(t)\cdot\frac{ds}{dt} \\ &= \frac{dZ}{dt}\cdot s(t) + Z(t)\cdot A(t)\, s(t) \\ &= \frac{dZ}{dt}\cdot s(t) + A(t)^T Z(t)\cdot s(t) \\ &= \left[\frac{dZ}{dt} + A(t)^T Z(t)\right]\cdot s(t) = (-L^* Z)(t)\cdot s(t)\,. \end{aligned} \tag{38}$$

Since the perturbation $s(t)$ is arbitrary, $Z(t)$ must be necessarily a solution of the adjoint operator (34).

Let us focus now on the normalization condition. Because of the definition of phase map that we have given, $\Theta(x(t)) = \theta$ for $\theta \in [0, T^*)$, the phase variation in time is constant equal 1. Then, it is clear that

$$1 = \frac{d\theta}{dt} = \nabla\Theta(x(t)) \cdot \frac{dx}{dt} = Z(t)\cdot F(x(t))\,, \tag{39}$$

being $x(t)$ the solution on the limit cycle.

□

To find a periodic solution of the adjoint equation (19) is, a priori, not straightforward. A possible way of computing a periodic orbit is to find a root of the map $P(z) = \phi_{T^*}(z) - z$, being T^* the period of the limit cycle, either using, for instance, a bisection method (easier to implement) or a Newton's method (faster but not as easy to implement).

Another possibility is to exploit the stability of the limit cycle. First, notice that the periodic solution that we are interested in is unstable as the minus sign in the right-hand side of (19) reverses the stability. Backward integration from any arbitrary point allows us to tend to that solution.

Here, however, we present an alternative method that is more convenient, computationally speaking, as it avoids seeking for a root of a map or integrating backwards, which overall is not numerically robust.

Alternative to solve Adjoint Equations: Let us consider the following Cauchy problem (similar in structure to the first variational equations)

$$\begin{cases} \dfrac{d}{dt}\psi(t) = -D_x F^T(\gamma(t))\,\psi(t)\,, \\ \psi(0) = Id\,, \end{cases} \tag{40}$$

where now, unlike the adjoint method, $\psi(t)$ is an $n \times n$ matrix. As before, this must be integrated simultaneously with the original system. Consider now the monodromy matrix $\psi(T^*)$ (i.e. the solution after a period). As our system has a periodic solution, then there must be an eigenvalue equal to 1. Let v_1 its eigenvector. Then, the infinitesimal PRC is given by the expression:

$$Z(t) = \frac{1}{\langle \psi(t)v_1, F(\gamma(t)) \rangle} \psi(t)v_1 \,, \tag{41}$$

where $\langle \cdot, \cdot \rangle$ is the usual Euclidean inner product (the deduction of this alternative method can be found in [9]).

So, from a numerical point of view, this alternative to the adjoint method is much more efficient as we only have to integrate a "first order system of variational equations" with the usual initial conditions.

Both methods require the differential of the vector field F, $D_xF(x)$, evaluated at the limit cycle. In our context, the system (8) - (9) is 8-dimensional with the following jacobian matrix

$$D_xF(x) = \begin{array}{c} \begin{matrix} \mathbf{r_e} & \mathbf{V_e} & \mathbf{S_{ee}} & \mathbf{S_{ei}} & \mathbf{r_i} & \mathbf{V_i} & \mathbf{S_{ie}} & \mathbf{S_{ii}} \end{matrix} \\ \begin{pmatrix} \frac{2V_e}{\tau_e} & \frac{2r_e}{\tau_e} & 0 & 0 & 0 & 0 & 0 & 0 \\ -\frac{2\tau_e^2\pi^2 r_e}{\tau_e} & \frac{2V_e}{\tau_e} & 1 & -1 & 0 & 0 & 0 & 0 \\ \frac{J_{ee}}{\tau_{s_e}} & 0 & -\frac{1}{\tau_{s_e}} & 0 & 0 & 0 & 0 & 0 \\ 0 & 0 & 0 & -\frac{1}{\tau_{s_e}} & \frac{J_{ei}}{\tau_{s_e}} & 0 & 0 & 0 \\ 0 & 0 & 0 & 0 & \frac{2V_i}{\tau_i} & \frac{2r_i}{\tau_i} & 0 & 0 \\ 0 & 0 & 0 & 0 & -\frac{2\tau_i^2\pi^2 r_i}{\tau_i} & \frac{2V_i}{\tau_i} & 1 & -1 \\ \frac{J_{ie}}{\tau_{s_i}} & 0 & 0 & 0 & 0 & 0 & -\frac{1}{\tau_{s_i}} & 0 \\ 0 & 0 & 0 & 0 & \frac{J_{ii}}{\tau_{s_i}} & 0 & 0 & -\frac{1}{\tau_{s_i}} \end{pmatrix} \end{array}.$$

B. Continuation method

To compute the boundaries of the Arnold tongues, we have used a continuation method based on a minimization problem with an additional restriction. In this Section we review the method presented in [13] and we adapt it to our setting.

Let $G : \mathbb{R}^n \times \mathbb{R} \to \mathbb{R}$ and consider the equation $G(\mathbf{u}, \lambda) = 0$, with $\mathbf{u}$ the set of variables and λ a real parameter. We will treat both parameters and variables equally and consider instead $G(w) = 0$, with $w = (\mathbf{u}, \lambda)$. Notice that this corresponds to a system with n nonlinear equations with $n+1$ variables. Parameters can always be treated as variables including the trivial ODE $\dot{\lambda} = 0$. If the rank of DG is maximal (i.e. $\text{rank}(DG(w)) = n$), by the Implicit Function Theorem, there exists a unique one-dimensional manifold parametrized by one of the components of w. The continuation method consists in two steps:

- **Prediction**: Let us suppose that w is a point lying on the saddle-node curve (i.e. $G(w) = 0$). We predict a new value by advancing a small quantity Δs along the tangent space at w. Since $\text{rank}(DG)$ is maximal the nullspace has dimension 1 and the tangent space is just a 1-dimensional manifold. Let A_k be the determinant of $DG(w)$ after removing the k-th column times $(-1)^{k-1}$. These determinants are well-defined since DG has maximal rank. We define the tangent line at w as the space spanned by the unitary vector

$$\mathbf{t} = \frac{1}{\sqrt{\sum_{i=1}^{n+1} A_i^2}} \left(A_1, A_2, \dots, A_n, A_{n+1}\right) \in \text{Ker}(DG(w)) \,. \tag{42}$$

  We make a prediction along the tangent of the form $w^* = w + \Delta s\, \mathbf{t}$, which, provided Δs is sufficiently small, is close to the saddle-node curve. We carry on with the corrective Newton-like method.

- **Correction**: Let w^* be an approximated solution of the saddle-node curve with $G(w^*) \approx 0$. We look for increments $\Delta w \in \mathbb{R}^n$ to refine the solution w^* successively. We Taylor expand $G(w^* + \Delta w)$ about w^* and we have

$$G(w^* + \Delta w) = G(w^*) + DG(w^*)\Delta w + \mathcal{O}(\|\Delta w\|_2^2) \,. \tag{43}$$

  This problem then reduces to find local extrema of the function $\|\Delta w\|_2^2$ conditioned to the submanifold $G(w^*) + DG(w^*)\Delta w = 0$. The associated Lagrangian function is

$$L(\Delta w, \mu) = \|\Delta w\|_2^2 + \mu^\top (G(w^*) + DG(w^*)\Delta w) \,, \tag{44}$$

  where $\mu \in \mathbb{R}$ (as many multipliers as the number of restrictions defining the submanifold). The local extrema of the above equation fulfills

$$\begin{aligned} &\frac{\partial L}{\partial (\Delta w)} = 2(\Delta w)^\top + \mu^\top DG(w^*) = 0 \quad \textbf{(Extrema condition)} \,, \\ &\frac{\partial L}{\partial \mu} = G(w^*) + DG(w^*)\Delta w = 0 \quad \textbf{(Submanifold condition)} \,. \end{aligned} \tag{45}$$

  Extrema condition gives the following expression for Δw

$$\Delta w = -\frac{1}{2} DG^\top(w^*)\mu \,. \tag{46}$$

Multiplying from the left both sides of equation (46) by the matrix $DG(w^*)$, and applying the condition of being on the submanifold, we have

$$\underbrace{DG(w^*)\Delta w}_{-G(w^*)} = -\frac{1}{2} DG(w^*)DG^\top(w^*)\mu \quad \Longrightarrow \quad \mu = 2\big(DG(w^*)DG^\top(w^*)\big)^{-1} G(w^*)\,. \tag{47}$$

Notice that in the latter equality we assume that the matrix product $DG(w^*)DG^\top(w^*)$ is invertible, which is true provided the number of equations is different from that of unknowns and the rank(DG) is maximal. Plugging expression (47) in equation (46), we have

$$\Delta w = -DG^\top(w^*)\big(DG(w^*)DG^\top(w^*)\big)^{-1} G(w^*)\,, \tag{48}$$

which improves the solution w^* and minimizes the Euclidean norm.

In summary, given an initial seed $w^0 := w^*$, the numerical algorithm performs as

$$w^{n+1} = w^n - DG^\top(w^n)\big(DG(w^n)DG^\top(w^n)\big)^{-1} G(w^n)\,, \tag{49}$$

with an stopping criteria that controls whether the norm $G(w^n)$ is smaller than a certain tolerance.

C. Computation of the differential matrix using variational equations

In this Section we present the method to compute the differential matrix of G (introduced in (26)), using variational equations. To do so, we treat T and A as variables and consider the extended non-autonomous system

$$\dot{w} = F(w,t) \Longleftrightarrow \begin{cases} \dot{\theta} = 1 + AZ(\theta)\cdot p(t)\,, \\ \dot{T} = 0\,, \\ \dot{A} = 0\,, \end{cases} \tag{50}$$

where $w = (\theta, T, A)$. Let $\psi_t(w, t_0) = \psi_t(\theta, T, A, t_0) := (\widetilde{\Phi}_t(\theta, T, A, t_0) \mod T^*, T, A)$ be the solution such that

$$\begin{cases} \dfrac{d}{dt}\psi_t(w,t_0) = F(\psi_t(w,t_0),t)\,, \\ \psi_{t_0}(w,t_0) = w_0\,, \end{cases} \tag{51}$$

where $w_0 = (\theta_0, T_0, A_0)$. Since the system is non-autonomous, $\widetilde{\Phi}_t$ (and thus ψ_t) depends on the initial integration time t_0. For the sake of completeness we have included it in the definition of ψ_t, however, from this point on, we will suppose $t_0 = 0$ and omit it. Moreover, even if variables T and A are constant over time and equal to T_0 and A_0, respectively, to what follows we keep calling them T and A.

Computing the matrix DG means determining the first and second partial derivatives of the extended flow $\widetilde{\Phi}_T(\theta, T, A)$. In the theory of differential equations, the dynamics of the derivatives (with respect to initial conditions) of the solution of a general Cauchy problem are provided by the so-called variational equations. The first variationals of the non-autonomous system (50) is the following homogeneous linear system of nine differential equations (with identity matrix as initial condition) whose solutions are the first derivatives of $\psi_t(w)$

$$\begin{aligned} \frac{d}{dt}\begin{pmatrix} \frac{\partial\psi^{(1)}}{\partial\theta} & \frac{\partial\psi^{(1)}}{\partial T} & \frac{\partial\psi^{(1)}}{\partial A} \\ \frac{\partial\psi^{(2)}}{\partial\theta} & \frac{\partial\psi^{(2)}}{\partial T} & \frac{\partial\psi^{(2)}}{\partial A} \\ \frac{\partial\psi^{(3)}}{\partial\theta} & \frac{\partial\psi^{(3)}}{\partial T} & \frac{\partial\psi^{(3)}}{\partial A} \end{pmatrix} &= \begin{pmatrix} D_\theta F_1 & D_T F_1 & D_A F_1 \\ D_\theta F_2 & D_T F_2 & D_A F_2 \\ D_\theta F_3 & D_T F_3 & D_A F_3 \end{pmatrix}\Bigg|_{\psi_t(w)} \begin{pmatrix} \frac{\partial\psi^{(1)}}{\partial\theta} & \frac{\partial\psi^{(1)}}{\partial T} & \frac{\partial\psi^{(1)}}{\partial A} \\ \frac{\partial\psi^{(2)}}{\partial\theta} & \frac{\partial\psi^{(2)}}{\partial T} & \frac{\partial\psi^{(2)}}{\partial A} \\ \frac{\partial\psi^{(3)}}{\partial\theta} & \frac{\partial\psi^{(3)}}{\partial T} & \frac{\partial\psi^{(3)}}{\partial A} \end{pmatrix} \\ &= \begin{pmatrix} D_\theta F_1 & D_T F_1 & D_A F_1 \\ 0 & 0 & 0 \\ 0 & 0 & 0 \end{pmatrix}\Bigg|_{\psi_t(w)} \begin{pmatrix} \frac{\partial\psi^{(1)}}{\partial\theta} & \frac{\partial\psi^{(1)}}{\partial T} & \frac{\partial\psi^{(1)}}{\partial A} \\ \frac{\partial\psi^{(2)}}{\partial\theta} & \frac{\partial\psi^{(2)}}{\partial T} & \frac{\partial\psi^{(2)}}{\partial A} \\ \frac{\partial\psi^{(3)}}{\partial\theta} & \frac{\partial\psi^{(3)}}{\partial T} & \frac{\partial\psi^{(3)}}{\partial A} \end{pmatrix}, \end{aligned}$$

where $(\psi^{(1)}, \psi^{(2)}, \psi^{(3)}) = (\widetilde{\Phi}_t(\theta, T, A) \mod T^*, T, A)$. The above system (as any other higher order system of variational equations) has been derived by differentiating $\frac{d}{dt}(\psi_t(w)) = F(\psi_t(w), t)$ with respect to w.

From all these time derivatives we are interested in those concerning partial derivatives of $\psi^{(1)}$ (evaluated at time T) because they are involved in the differential of the extended stroboscopic map (25). Since the matrix DF has two zero rows, the final system to be solved simplifies significantly and is given by

$$\begin{aligned}
\frac{d}{dt}\frac{\partial\psi^{(1)}}{\partial\theta} &= D_\theta F_1(\psi_t(w),t)\frac{\partial\psi^{(1)}}{\partial\theta} + D_T F_1(\psi_t(w),t)\frac{\partial\psi^{(2)}}{\partial\theta} + D_A F_1(\psi_t(w),t)\frac{\partial\psi^{(3)}}{\partial\theta}\,,\\
\frac{d}{dt}\frac{\partial\psi^{(1)}}{\partial T} &= D_\theta F_1(\psi_t(w),t)\frac{\partial\psi^{(1)}}{\partial T} + D_T F_1(\psi_t(w),t)\frac{\partial\psi^{(2)}}{\partial T} + D_A F_1(\psi_t(w),t)\frac{\partial\psi^{(3)}}{\partial T}\,,\\
\frac{d}{dt}\frac{\partial\psi^{(1)}}{\partial A} &= D_\theta F_1(\psi_t(w),t)\frac{\partial\psi^{(1)}}{\partial A} + D_T F_1(\psi_t(w),t)\frac{\partial\psi^{(2)}}{\partial A} + D_A F_1(\psi_t(w),t)\frac{\partial\psi^{(3)}}{\partial A}\,.
\end{aligned} \tag{52}$$

Moreover since $\psi^{(2)} = T$ and $\psi^{(3)} = A$, equations (52) reduce to

$$\begin{aligned}
\frac{d}{dt}\frac{\partial\psi^{(1)}}{\partial\theta} &= D_\theta F_1(\psi_t(w),t)\frac{\partial\psi^{(1)}}{\partial\theta}\,,\\
\frac{d}{dt}\frac{\partial\psi^{(1)}}{\partial T} &= D_\theta F_1(\psi_t(w),t)\frac{\partial\psi^{(1)}}{\partial T} + D_T F_1(\psi_t(w),t)\,,\\
\frac{d}{dt}\frac{\partial\psi^{(1)}}{\partial A} &= D_\theta F_1(\psi_t(w),t)\frac{\partial\psi^{(1)}}{\partial A} + D_A F_1(\psi_t(w),t)\,.
\end{aligned} \tag{53}$$

From now on, as we only care about the partial derivatives of the component $\psi^{(1)}$ of $\psi_t(w)$, we will simply refer to it as $\widetilde{\Phi}_t(\theta, T, A)$ (or shorter as $\widetilde{\Phi}_t(w)$).

The solution of the above system of equations determines the derivatives of the fixed point condition $\widetilde{P}(\theta, T, A) - \theta$ with respect to θ, T and A. Hence, the first row of the differential matrix of G (system of equations (26)) is given by the first variational equations. On the other hand, the derivatives of the saddle-node condition $\frac{\partial\widetilde{P}}{\partial\theta} - 1$ are provided by the second order variational equations. The most straightforward way to figure them out is by differentiating equations (53) with respect to $w = (\theta, T, A)$ and exchanging time and spatial derivatives. In fact, we do not need all the second derivatives rather those concerning the partial derivative of $\widetilde{\Phi}_t$ with respect to θ. Using the chain rule, we differentiate the first equation in (53) with respect to (θ, T, A) and we have:

$$\frac{d}{dt}\frac{\partial^2\widetilde{\Phi}}{\partial\theta^2} = \left[D_{\theta\theta}F_1(\psi_t(w),t)\frac{\partial\widetilde{\Phi}}{\partial\theta}\right]\frac{\partial\widetilde{\Phi}}{\partial\theta} + D_\theta F_1(\psi_t(w),t)\frac{\partial^2\widetilde{\Phi}}{\partial\theta^2}$$

$$= D_{\theta\theta}F_1(\psi_t(w),t)\Big(\frac{\partial\widetilde{\Phi}}{\partial\theta}\Big)^2 + D_\theta F_1(\psi_t(w),t)\frac{\partial^2\widetilde{\Phi}}{\partial\theta^2}\,,$$

$$\frac{d}{dt}\frac{\partial^2\widetilde{\Phi}}{\partial T\partial\theta} = \left[D_{\theta\theta}F_1(\psi_t(w),t)\frac{\partial\widetilde{\Phi}}{\partial T} + D_{T\theta}F_1(\psi_t(w),t)\right]\frac{\partial\widetilde{\Phi}}{\partial\theta} + D_\theta F_1(\psi_t(w),t)\frac{\partial^2\widetilde{\Phi}}{\partial T\partial\theta}$$

$$= D_{\theta\theta}F_1(\psi_t(w),t)\frac{\partial\widetilde{\Phi}}{\partial T}\frac{\partial\widetilde{\Phi}}{\partial\theta} + D_{T\theta}F_1(\psi_t(w),t)\frac{\partial\widetilde{\Phi}}{\partial\theta} + D_\theta F_1(\psi_t(w),t)\frac{\partial^2\widetilde{\Phi}}{\partial T\partial\theta}\,,$$

$$\frac{d}{dt}\frac{\partial^2\widetilde{\Phi}}{\partial A\partial\theta} = \left[D_{\theta\theta}F_1(\psi_t(w),t)\frac{\partial\widetilde{\Phi}}{\partial A} + D_{A\theta}F_1(\psi_t(w),t)\right]\frac{\partial\widetilde{\Phi}}{\partial\theta} + D_\theta F_1(\psi_t(w),t)\frac{\partial^2\widetilde{\Phi}}{\partial A\partial\theta}$$

$$= D_{\theta\theta}F_1(\psi_t(w),t)\frac{\partial\widetilde{\Phi}}{\partial A}\frac{\partial\widetilde{\Phi}}{\partial\theta} + D_{A\theta}F_1(\psi_t(w),t)\frac{\partial\widetilde{\Phi}}{\partial\theta} + D_\theta F_1(\psi_t(w),t)\frac{\partial^2\widetilde{\Phi}}{\partial A\partial\theta}\,.$$

In the general case the second variational equations should be integrated along with the first ones and the original system, bringing a system of n^3+n^2+n differential equations (a total of 39 equations when $n=3$). Nonetheless, in our particular case the number of equations has been reduced to solve a system of only seven ODEs given by

$$\begin{cases}
\dfrac{d\theta}{dt} = 1 + AZ(\theta)\cdot p(t)\,,\\[2ex]
\dfrac{d}{dt}\dfrac{\partial\widetilde{\Phi}}{\partial\theta} = D_\theta F_1(\psi_t(w),t)\dfrac{\partial\widetilde{\Phi}}{\partial\theta}\,,\\[2ex]
\dfrac{d}{dt}\dfrac{\partial\widetilde{\Phi}}{\partial T} = D_\theta F_1(\psi_t(w),t)\dfrac{\partial\widetilde{\Phi}}{\partial T} + D_T F_1(\psi_t(w),t)\,,\\[2ex]
\dfrac{d}{dt}\dfrac{\partial\widetilde{\Phi}}{\partial A} = D_\theta F_1(\psi_t(w),t)\dfrac{\partial\widetilde{\Phi}}{\partial A} + D_A F_1(\psi_t(w),t)\,,\\[2ex]
\dfrac{d}{dt}\dfrac{\partial^2\widetilde{\Phi}}{\partial\theta^2} = D_{\theta\theta}F_1(\psi_t(w),t)\Big(\dfrac{\partial\widetilde{\Phi}}{\partial\theta}\Big)^2 + D_\theta F_1(\psi_t(w),t)\dfrac{\partial^2\widetilde{\Phi}}{\partial\theta^2}\,,\\[2ex]
\dfrac{d}{dt}\dfrac{\partial^2\widetilde{\Phi}}{\partial T\partial\theta} = D_{\theta\theta}F_1(\psi_t(w),t)\dfrac{\partial\widetilde{\Phi}}{\partial T}\dfrac{\partial\widetilde{\Phi}}{\partial\theta} + D_{T\theta}F_1(\psi_t(w),t)\dfrac{\partial\widetilde{\Phi}}{\partial\theta} + D_\theta F_1(\psi_t(w),t)\dfrac{\partial^2\widetilde{\Phi}}{\partial T\partial\theta}\,,\\[2ex]
\dfrac{d}{dt}\dfrac{\partial^2\widetilde{\Phi}}{\partial A\partial\theta} = D_{\theta\theta}F_1(\psi_t(w),t)\dfrac{\partial\widetilde{\Phi}}{\partial A}\dfrac{\partial\widetilde{\Phi}}{\partial\theta} + D_{A\theta}F_1(\psi_t(w),t)\dfrac{\partial\widetilde{\Phi}}{\partial\theta} + D_\theta F_1(\psi_t(w),t)\dfrac{\partial^2\widetilde{\Phi}}{\partial A\partial\theta}\,,
\end{cases} \tag{54}$$

with $\psi_t(w) = (\widetilde{\Phi}_t(\theta,T,A) \bmod T^*, T, A)$ the flow of the original extended system (50). The initial condition so as to integrate the above system of ODEs is

$$x_0 = \left(\theta\,,\ \frac{\partial\widetilde{\Phi}}{\partial\theta}\,,\ \frac{\partial\widetilde{\Phi}}{\partial T}\,,\ \frac{\partial\widetilde{\Phi}}{\partial A}\,,\ \frac{\partial^2\widetilde{\Phi}}{\partial\theta^2}\,,\ \frac{\partial^2\widetilde{\Phi}}{\partial T\partial\theta}\,,\ \frac{\partial^2\widetilde{\Phi}}{\partial A\partial\theta}\right) = (\theta_0\,,\ 1\,,\ 0\,,\ 0\,,\ 0\,,\ 0\,,\ 0)\,,$$

where θ_0 is the first component of the initial condition of the Cauchy problem (51). The other components of x_0 come from the initial conditions of the first and second variational Cauchy problems.

We now focus on the computation of the partial derivatives of the function $F_1(w,t) = 1 + AZ(\theta)\cdot p(t)$. Recall that the external (non-negative) periodic perturbation is of the form $p(t) = 1 + \cos\left(\frac{2\pi t}{T}\right)$. We note that the perturbation $p(t)$ depends on T. Thus,

$$
\begin{aligned}
D_\theta F_1(w,t) &= A\,Z'(\theta)\left(1+\cos\Big(\frac{2\pi t}{T}\Big)\right), & D_{\theta\theta} F_1(w,t) &= A\,Z''(\theta)\left(1+\cos\Big(\frac{2\pi t}{T}\Big)\right),\\
D_T F_1(w,t) &= \frac{2\pi t}{T^2} A\,Z(\theta)\sin\Big(\frac{2\pi t}{T}\Big), & D_{T\theta} F_1(w,t) &= \frac{2\pi t}{T^2} A\,Z'(\theta)\sin\Big(\frac{2\pi t}{T}\Big),\\
D_A F_1(w,t) &= Z(\theta)\left(1+\cos\Big(\frac{2\pi t}{T}\Big)\right), & D_{A\theta} F_1(w,t) &= Z'(\theta)\left(1+\cos\Big(\frac{2\pi t}{T}\Big)\right),
\end{aligned}
$$

Notice that, the first and second derivatives of the linear response $Z(\theta)$ are required. In our current study there is no analytical expression for $Z(\theta)$ but rather a discrete form (by numerical integration of the system (40)). Under some regularity hypothesis (namely $Z(\theta) \in L_2([0,T^*])$ one may express the T^*-periodic function $Z(\theta)$ as a complex exponential Fourier series

$$
Z(\theta) = \sum_{k=-\infty}^{\infty} c_k e^{\frac{2\pi i k\theta}{T^*}}, \quad \text{with} \quad c_k = \frac{1}{T^*}\int_0^{T^*} Z(\theta) e^{-\frac{2\pi i|k|\theta}{T^*}} d\theta\,. \tag{55}
$$

Assuming that $Z(\theta)$ is at least C^2, we are allowed to take first and second derivatives with respect to θ on both sides of the above Fourier series. The exponential form of the above series helps us to write the first derivative in a clear style

$$
Z'(\theta) = \sum_{k=-\infty}^{\infty} c'_k e^{\frac{2\pi i k\theta}{T^*}}, \quad \text{with} \quad c'_k = 2\pi i k\, c_k\,. \tag{56}
$$

Analogously one can check that the Fourier coefficients for the second derivative $Z''(\theta)$ are $c''_k = 2\pi i k\, c'_k$. In practice we have to compute such coefficients c_k of Z using the discrete Fourier transform

$$
c_k = \sum_{n=0}^{N-1} Z_n e^{-\frac{2\pi i k n}{N}}, \qquad k = 0,\dots,N-1\,, \tag{57}
$$

where $\{Z_n\}_{n=0}^{N-1}$ is an equidistant discrete sequence of N values of the infinitesimal PRC, $Z(\theta)$. Numerically, this has been implemented using the Matlab built-in function `fft` (fast fourier algorithm) and the inverse `ifft` to recover a discrete form of Z' and Z''. In Figure 22 we display the derivatives of the phase response curve $Z(\theta)$ obtained using the fast Fourier transform `fft` for each one of the cases that we explore.

Once we have solved numerically the first and second order variational equations, we proceed to construct the matrix DG. Recall that the function G, characterizing the Arnold tongue boundary, is given by

$$
G(w) = \begin{pmatrix} \widetilde{\Phi}_T(\theta,T,A) - \theta \\ \dfrac{\partial \widetilde{\Phi}_T}{\partial\theta}(\theta,T,A) - 1 \end{pmatrix}, \tag{58}
$$

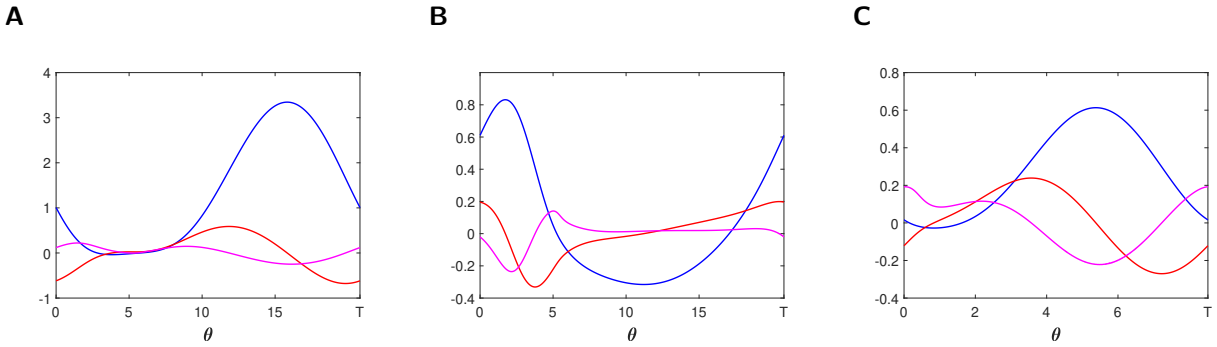

Figure 22: Infinitesimal phase response curve $Z(\theta)$ (blue curve) and its first and second derivatives (red and magenta curves, respectively) using the discrete Fourier transform for: (**A**) PING interplay perturbing the variable V_e, (**B**) PING interplay perturbing the variable V_i and (**C**) ING interplay perturbing the variable V_i.

where, as stated previously, $\widetilde{\Phi}_t(\theta, T, A)$ is the extended flow of the phase equation (21) when T and A are treated as variables. Notice that we are evaluating the flow at time $t = T$. Thus, the derivatives with respect to T must be treated with caution as T appears twice, in the spatial and time variables. We have

$$\begin{aligned}
\frac{\partial}{\partial T}\big(\widetilde{\Phi}_T(\theta, T, A)\big) &= \left\{\frac{d}{dt}\big(\widetilde{\Phi}_t(\theta, T, A)\big) + \frac{\partial \widetilde{\Phi}_t}{\partial T}(\theta, T, A)\right\}\Big|_{t=T} \\
&= F_1(\psi_T(w), T) + \frac{\partial \widetilde{\Phi}_T}{\partial T}(\theta, T, A)\,, \\
\frac{\partial}{\partial T}\Big(\frac{\partial \widetilde{\Phi}_T}{\partial \theta}\Big)(\theta, T, A) &= \left\{\frac{d}{dt}\Big(\frac{\partial \widetilde{\Phi}_t}{\partial \theta}\Big)(\theta, T, A) + \frac{\partial^2 \widetilde{\Phi}_t}{\partial T \partial \theta}(\theta, T, A)\right\}\Big|_{t=T} \\
&= D_\theta F_1(\psi_T(w), T)\frac{\partial \widetilde{\Phi}_T}{\partial \theta}(\theta, T, A) + \frac{\partial^2 \widetilde{\Phi}_T}{\partial T \partial \theta}(\theta, T, A)\,,
\end{aligned} \tag{59}$$

and therefore, the matrix DG is given by

$$DG(w) = \begin{pmatrix} \dfrac{\partial \widetilde{\Phi}_T}{\partial \theta}(w) - 1 & F_1(\psi_T(w), T) + \dfrac{\partial \widetilde{\Phi}_T}{\partial T}(w) & \dfrac{\partial \widetilde{\Phi}_T}{\partial A}(w) \\ \dfrac{\partial^2 \widetilde{\Phi}_T}{\partial \theta^2}(w) & D_\theta F_1(\psi_T(w), T)\dfrac{\partial \widetilde{\Phi}_T}{\partial \theta}(w) + \dfrac{\partial^2 \widetilde{\Phi}_T}{\partial T \partial \theta}(w) & \dfrac{\partial^2 \widetilde{\Phi}_T}{\partial A \partial \theta}(w) \end{pmatrix}.$$

In the most general framework, the function G, defining the boundary of a $1 : q$ Arnold tongue, is similar to the equations (58) where, again, we regard T and A as variables (that is, we consider the extended flow $\widetilde{\Phi}_t$ and its associated stroboscopic map (25))

$$G(w) = \begin{pmatrix} \widetilde{\Phi}_{qT}(\theta, T, A) - \theta \\ \dfrac{\partial \widetilde{\Phi}_{qT}}{\partial \theta}(\theta, T, A) - 1 \end{pmatrix}. \tag{60}$$

Notice that the extended flow $\widetilde{\Phi}_t$ is integrated up to qT. The matrix DG has almost the same structure as in the $1:1$ Arnold tongue, except that system (54) must now be integrated up to a larger time qT. This entails an extra term in the derivatives with respect to T (not present in equations (59)).

$$\begin{aligned}
\frac{\partial}{\partial T}\big(\widetilde{\Phi}_{qT}(\theta, T, A)\big) &= \left\{ \frac{d}{dt}\big(\widetilde{\Phi}_t(\theta, T, A)\big)\, q + \frac{\partial \widetilde{\Phi}_t}{\partial T}(\theta, T, A) \right\}\Big|_{t=qT} \\
&= q\, F_1(\psi_{qT}(w), qT) + \frac{\partial \widetilde{\Phi}_{qT}}{\partial T}(\theta, T, A)\,, \\
\frac{\partial}{\partial T}\Big(\frac{\partial \widetilde{\Phi}_{qT}}{\partial \theta}\Big)(\theta, T, A) &= \left\{ \frac{d}{dt}\Big(\frac{\partial \widetilde{\Phi}_t}{\partial \theta}\Big)(\theta, T, A)\, q + \frac{\partial^2 \widetilde{\Phi}_t}{\partial T \partial \theta}(\theta, T, A) \right\}\Big|_{t=qT} \\
&= q\, D_\theta F_1(\psi_{qT}(w), qT) \frac{\partial \widetilde{\Phi}_{qT}}{\partial \theta}(\theta, T, A) + \frac{\partial^2 \widetilde{\Phi}_{qT}}{\partial T \partial \theta}(\theta, T, A)\,.
\end{aligned} \tag{61}$$

The matrix DG has therefore the following form

$$DG(w) = \begin{pmatrix} \dfrac{\partial \widetilde{\Phi}_{qT}}{\partial \theta}(w) - 1 & q\, F_1(\psi_{qT}(w), qT) + \dfrac{\partial \widetilde{\Phi}_{qT}}{\partial T}(w) & \dfrac{\partial \widetilde{\Phi}_{qT}}{\partial A}(w) \\ \dfrac{\partial^2 \widetilde{\Phi}_{qT}}{\partial \theta^2}(w) & q\, D_\theta F_1(\psi_{qT}(w), qT) \dfrac{\partial \widetilde{\Phi}_{qT}}{\partial \theta}(w) + \dfrac{\partial^2 \widetilde{\Phi}_{qT}}{\partial T \partial \theta}(w) & \dfrac{\partial^2 \widetilde{\Phi}_{qT}}{\partial A \partial \theta}(w) \end{pmatrix}.$$